

Numerical modeling of stresses and deformation in Zagros-Iranian plateau region

Srishti Singh¹ and Radheshyam Yadav¹

¹ CSIR-National Geophysical Research Institute, Hyderabad, India-500007

Key Points

- We have computed stresses and deformation of Zagros-Iran region with finite element modeling.
- Lithospheric stresses play an important role in the east of Iran.
- The joint models of lithosphere and mantle convection are able to explain various deformation indicators in the study area.

Abstract

Zagros orogeny System resulted due to collision of the Arabian plate with the Eurasian plate. The region has the ocean-continent subduction and continent-continent collision; and convergence velocity shows variation from east to west. Therefore, this region shows the complex tectonic stress and a wide range of diffuse or localized deformation between both plates. The in-situ stress and GPS data are very limited and sparsely distributed in this region, therefore, we performed a numerical simulation of the stresses causing deformation in the Zagros-Iran region. The deviatoric stresses resulting from the variations in lithospheric density and thickness; and those from shear tractions at the base of the lithosphere due to mantle convection were computed using thin-sheet approximation. Stresses associated with both sources can explain various surface observations of strain rates, S_{Hmax} , and plate velocities; thus, Surface observations of strain rates, S_{Hmax} , plate velocities etc. are explained using the joint models of lithosphere and mantle, suggesting a good coupling between lithosphere and mantle in most parts of Zagros and Iran. As the magnitude of stresses due to shear tractions from density-driven mantle convection is higher than those from lithospheric density and topography variations in the Zagros-Iranian plateau region, mantle convection appears to be the dominant driver of deformation in this area. However, the deformation in the east of Iran is caused primarily by lithospheric stresses. The plate velocity of the Arabian plate is found to vary along the Zagros belt from north-northeast in the southeast of Zagros to the northwest in the northwestern Zagros, similar

28 to observed GPS velocity vectors Plate motion of Arabian plate is found to vary along the Zagros
29 belt from north-northeast in south-east of Zagros, north in central Zagros to slight northwest in the
30 northwestern Zagros. The output of this study can be used in seismic hazards estimations.

31 **Keywords-** Stress field, Gravitational Potential Energy, Mantle convection, Zagros, collision

32 Plain Language Summary

33 We used numerical models to study the stresses causing deformation in the Zagros-Iran region. The
34 stresses are generated due to variations in the density and topography of the lithosphere, which were
35 computed through Gravitational potential energy (GPE) difference. Mantle convection produces shear
36 tractions that are also an important source of stresses causing deformation. Different models of crustal
37 structure and density of lithosphere give varying GPE, thus leading to different interpretations of the type
38 of deformation in the study area. On the other hand, all mantle convection models in our study predicted
39 consistent deviatoric stresses and were able to explain most observations of S_{Hmax} , plate velocities, and
40 strain rates. Despite this, the lithosphere plays an important role in driving deformation, especially in
41 the east of Iran. Overall, the lithospheric stresses when combined with those from mantle convection
42 gave the best fit to the observed data.

43 1 Introduction

44 Zagros mountains are a part of the Alpine-Himalayan belts that originated due to the Arabian plate
45 colliding with southern boundary of the Eurasian plate. This collision resulted from the in closing of
46 the Neotethys Ocean and formed Zagros fold and thrust belt (Agard et al., 2005, 2011; Alavi, 1980;
47 Mouthereau et al., 2012). The Zagros mountains extend from the eastern part of the Anatolia for over
48 1500 km in the NW-SE direction till the Makran subduction zone, showing large-scale diffuse deforma-
49 tion. Despite the first-order characteristics of Though there has been an increase in the influx of various
50 studies trying to constrain the active deformation and present-day kinematics of Zagros orogen is rela-
51 tively well understood (Allen et al., 2011; Le Dertz et al., 2009; Reilinger et al., 2010; Vernant et al.,
52 2004; Walker, 2006), there are debates about various processes in this region, e.g. the timing of the colli-
53 sion is debated. Various authors (Jolivet & Faccenna, 2000; Agard et al., 2005, 2011; Vincent et al., 2005; Ballato et
54 have suggested that collision onset time to be in Late Eocene to Oligocene; however, Timing of collision
55 ranges from Cretaceous (Alavi, 1994; Mohajel & Fergusson, 2000) to Miocene (Berberian & King,
56 1981) or Eocene (Allen & Armstrong, 2008; Jolivet & Faccenna, 2000). However, there has been an
57 increasing consensus on Late Eocene to Oligocene for the onset of collision (Jolivet & Faccenna, 2000;

58 Agard et al., 2005, 2011; Vincent et al., 2005; Ballato et al., 2011; Mouthereau et al., 2012; Koshnaw
59 et al., 2019). Ghalamghash et al. (2009); Mazhari et al. (2009) have argued Late Palaeocene or Early
60 Eocene for the onset of collision. The Zagros and its foreland area have a great source of natural
61 resources like petroleum. The study area consists of the ocean-continent subduction as well as the
62 continental collisions. The convergence rate of the Arabian plate relative to the Eurasia varies from
63 east to west (Figure 1). These complex structures and convergence velocity variation made the variable
64 tectonic stress and deformation. The geophysical, geological and geodesy studies show that these areas
65 are seismic active based on the earthquake data, fault slip rates and GPS velocities, which is related to
66 the complex stress field in this region. The Arabia-Eurasia collision zone is a tectonically active region,
67 where ongoing convergence is accommodated by distributed shortening across the Zagros Mountains
68 and the northern and eastern margins of the Iranian Plateau and the southern Caspian Sea. The rate
69 of convergence of Arabia relative to Eurasia also varies significantly, decreasing from 36 mm/yr in the
70 east to 16 mm/yr in the west (Figure 1). The diverse structures, tectonic history, and convergence ve-
71 locity variations in the Zagros-Iran plateau region lead to variable tectonic stresses and deformations,
72 thus making it the focus of various geophysical, geological, and geodesy studies (Engdahl et al., 2006;
73 Hatzfeld et al., 2010; Khorrami et al., 2019; Masson et al., 2006; Tunini et al., 2016, 2017). Based on
74 earthquake focal mechanisms, fault slip, and GPS velocities, the Zagros-Iran region has been catego-
75 rized as a highly seismic region; thus a better constraint on stresses and deformation in this region may
76 be helpful in disaster mitigation studies.

77 Generally, tectonic stress refers to the forces acting on the Earth's crust that cause it to deform or un-
78 dergo changes and it's classified by the first, second and third order on the spatial scale (Heidbach et al.,
79 2007; Zoback, 1992). The first-order stresses originate due to the plate boundaries force like ridge push,
80 slab pull and continental collisional; and second-order stresses by the rifting, isostasy and deglaciation.
81 Moreover, third-order stresses are caused by local sources like interaction faults systems, topography and
82 density heterogeneity. Therefore, to understand the origin of these stresses, in-situ stress measurements
83 are done using the focal mechanism inversion, wellbore breakouts, hydraulic fracturing and overcoring,
84 and compiled under the word stress map project. However, in-situ stress data are sparsely distributed and
85 limited, so numerical modeling plays an important role in understanding the kinematics and dynamics of
86 the Zagros-Iran region. Numerical modeling of tectonic stresses and deformation is generally conducted
87 in two approaches (1) using 2D and 3D geometrical structure, plate boundary forces like ridge push, slab
88 pull and continents collision forces and rheological properties like Young's modulus, Poisson's ratio, vis-
89 cosity, density etc. (Coblenz & Sandiford, 1994; Dyksterhuis & Müller, 2008; Koptev & Ershov, 2010;
90 Richardson et al., 1976; Yadav & Tiwari, 2018), and, (2) considering Gravitational Potential energy and
91 shear tractions from mantle convection with thin sheet approximation (Bird, 1998; Flesch et al., 2001;

92 Ghosh & Holt, 2012; Lithgow-Bertelloni & Guynn, 2004; Singh & Ghosh, 2020). Therefore, the world
93 stress map (WSM) provides in-situ stress measurement and the compilation from the focal mechanism,
94 hydrofracturing, and borehole breakout. However, the in-situ stress (WSM) and GPS velocity data
95 (ArRajehi et al., 2010; Bayer et al., 2006; Frohling & Szeliga, 2016; Khorrami et al., 2019; Masson et al., 2006,
96 are very limited and sparsely distributed in this region; therefore, there is need for a numerical simulation
97 study to comprehend the knowledge.

98 Although numerical modeling of tectonic stress and deformation was conducted in two approaches
99 (1) using 2D and 3D geometrical structure, plate boundary forces like ridge push, slab pull and continents
100 collision forces and rheological properties like Young's modulus, Poisson's ratio, viscosity, density
101 (Dyksterhuis & Müller, 2008; Coblenz et al., 1994; Koptev & Ershov, 2010; Richardson et al., 1976; Yadav & Ti
102 and, (2) considering Gravitational Potential energy and shear tractions from mantle convection with thin
103 sheet approximation (Bird, 1998; Lithgow-Bertelloni & Guynn, 2004; Flesch et al., 2001; Ghosh & Holt, 2012; Si
104 Stress studies showed that it's classified by the first, second and third order on the spatial scale (Zoback, 1992; Heid
105 The first-order stresses are originated due to the plate boundaries force like ridge push, slab pull and
106 continental collisional; and second-order stress by the rifting, isostasy and deglaciation. Moreover,
107 third-order stress are caused by local sources like interaction faults systems, topography and density
108 heterogeneity.

109 There are various studies that have tried to investigate present-day stresses and deformations of the
110 Zagros-Iranian plateau region using focal mechanism inversions, GPS data and numerical modeling.
111 The stresses were computed through the inversion of focal mechanisms in areas like the Zagros fold-
112 and-thrust belt (Nouri et al., 2023; Sarkarnejad et al., 2018; Yaghoubi et al., 2021), Zagros-Makran
113 transition zone (Ghorbani Rostam et al., 2018), western Zagros (Navabpour et al., 2008), NW Iran-
114 SE Turkey (Mokhori et al., 2021), NE Lut Block, Eastern Iran (Rashidi et al., 2022; Raeesi et al.,
115 2017), and the south Caspian (Jackson et al., 2002). The GPS studies also provide constraints on
116 the present-day deformation in Zagros-Makran transition zone (Bayer et al., 2006), Makran subduc-
117 tion zone (Frohling & Szeliga, 2016), Iran (Khorrami et al., 2019; Masson et al., 2006, 2007; Ver-
118 nant et al., 2004; Walpersdorf et al., 2014), Nubia–Arabia–Eurasia plate system (Reilinger & Mc-
119 Clusky, 2011).numerical studies conducted for tectonic stresses and deformation in Zagros-Iranian region
120 (Austermann & Iaffaldano, 2013; Md & Ryuichi, 2010; Francois et al., 2014; Khodaverdian et al., 2015; Vernant
121 Sobouti & Arkani-Hamed (1996) studied the large scale tectonic processes of the region and repro-
122 duced observed faulting patterns by considering highly rigid central Iran and the South Caspian Sea
123 using a viscous thin-sheet approximation. On the other hand, Md & Ryuichi (2010) used finite ele-
124 ment modeling (FEM) to analyse the neotectonic stress field of Zagros and adjoining area modelled
125 the maximum horizontal compressive stress (S_{Hmax}) orientations and showed N-S/NNE-SSW oriented

~~126 S_{Hmax} in Lurestan and eastern Zagros Simple Folded Belt, whereas they were aligned in NW-SE directions~~
~~127 around Main Recent fault (MRF) and in the northern High Zagros Faults (HZF). Sebouli & Arkani-Hamed (1996)~~
~~128 reproduced observed faulting patterns by considering highly rigid central Iran and the South Caspian~~
~~129 Sea using a viscous thin-sheet approximation. Further, the kinematic model by Khodaverdian et al.~~
~~130 (2015) provided~~ ~~provided~~ constraints on fault slip rates, plate velocities and seismicity of the Iranian
~~131 Plateau. Most of the deformation studies done in this region focus on different tectonic fragments~~
~~132 of the Arabia-Eurasia collision zone. Moreover, the previous studies do not include the role of shear~~
~~133 tractions associated with mantle convections in affecting the deformation and stresses in the Zagros-~~
~~134 Iran regions. The previous models did not include the mantle convections derived shear tractions for~~
~~135 computation of deformation and stress in the Zagros-Iran regions.~~

~~136 In this study, we investigate the stress and deformation in Zagros-Iranian Plateau region to constrain~~
~~137 the forces acting in this region with gravitational potential energy (GPE) and shear traction of mantle~~
~~138 tractions. We will use a thin viscous sheet model based on Flesch et al. (2001) to compute various de-~~
~~139 formation parameters such as deviatoric stresses, strain rates, most compressive principal stress (S_{Hmax}),~~
~~140 and plate velocities within the Zagros-Iran region.~~

~~141 2 Tectonic and Geology~~

~~142 The evolution~~ ~~rise~~ of the Zagros mountain belt is a direct consequence of continental collision between
~~143 the Arabian and Eurasian plates. Zagros are located at the northeastern margin of the Arabian plate,~~
~~144 trending in the southwest direction (Figure 1). It is bounded by the Main Zagros thrust (MZT) in the~~
~~145 northeast, while it joins the Tauras mountains in southern Turkey in the northwest. In the southeast, N-S~~
~~146 trending Minab-Zandan fault zone separates Zagros from the Makran range. Outer Zagros are the young~~
~~147 folded mountains in the southwest parts of the orogeny (Falcon, 1974; Sattarzadeh et al., 2002). High~~
~~148 Zagros fault (HZF) separates highly deformed metamorphic rocks of inner Zagros from Simply folded~~
~~149 mountains of outer Zagros (Hatzfeld & Molnar, 2010; Hatzfeld et al., 2010). Inner Zagros are bounded~~
~~150 by MZT in the northeast and are dominated by thrust faulting, possibly due to compression during the~~
~~151 Late Cretaceous (Alavi, 1980). The northwestern Zagros~~ ~~is~~ ~~are~~ separated from central Zagros by a north-
~~152 south trending strike-slip zone of deformation, known as Kazerun Fault System (KFS) (Authemayou~~
~~153 et al., 2005).~~

~~154 Zagros mountains were formed between ~35 and ~23 Ma due to the convergence of the Arabian~~
~~155 platform beneath the central Iranian crust (Agard et al., 2005; Ballato et al., 2011; Moutherneau et al.,~~
~~156 2012). The Arabian plate moves towards Eurasia with a plate velocity of 22-35 mm/yr (DeMets et al.,~~
~~157 1990; McClusky et al., 2000; Jackson et al., 2002; McQuarrie et al., 2003; Reilinger et al., 2006) in~~

158 N-S to NNE direction. Zagros mountain belt is also accompanied by The convergence of two rigid
159 plates of Arabia and Eurasia leads to a zone of widespread deformation in the form of the high plateaus
160 of Iran. Iranian plateau extends from the Caspian Sea and the Kopeh Dagh range in the north to the
161 Zagros Mountains in the west. Iranian plateau is bounded by the Persian Gulf and Hormuz Strait in
162 the south and the political borders of the country on the eastern side. Several tectonic processes such
163 as intracontinental collisions, subduction along the Makran and the transition from Zagros fold-thrust
164 belt to the Makran subduction zone contribute to the complex tectonics of the Iranian plateau. Numerous
165 earthquakes occur in these high terrains due to sustained tectonic activities; hence, these areas are prone
166 to large seismic hazards.

167 During the last few decades, various geophysical ~~studies~~ surveys (receiver functions, deep seismic,
168 GPS and tomographic) ~~studies~~ have been carried out in the Zagros-Iran region to investigate the ~~struc-~~
169 ~~ture and~~ deformation in this region. The southeastern Zagros accommodate the convergence between
170 Arabia and Eurasia by pure shortening occurring through high-angle ($30^\circ - 60^\circ$) reverse faults that are
171 perpendicular to the belt (Hessami et al., 2006; Irandoost et al., 2022; Walpersdorf et al., 2006). On
172 the other hand, oblique convergence in central and northern Zagros is partitioned into a strike-slip com-
173 ponent that is accommodated on MRF and shortening occurring across the belt (Jackson et al., 2002;
174 Talebian & Jackson, 2002). Zagros is separated from Makran subduction zone (MSZ) by Minab-Zendan-
175 Palami (MZP) fault ($54^\circ - 58^\circ E$), which is a right-lateral strike-slip fault (Bayer et al., 2006). East of
176 MZP shows significant shortening that is accommodated through the subduction in MSZ. Due to the
177 difference between convergence rates, a shearing occurs in eastern Iran which is accommodated by the
178 N-S trending faults bounding the Lut block. In northern Iran, fold and thrust belt of Alborz accommo-
179 dates a quarter of the Arabia-Eurasia convergence Irandoost et al. (2022). The oblique convergence in
180 eastern Alborz is also partitioned into shortening at the southern boundary and a left-lateral component
181 across the mountain belt (Irandoost et al., 2022; Khorrami et al., 2019; Tatar & Hatzfeld, 2009). Alborz
182 mountains extend into Talesh in the west which shows ~~s~~ thrust faulting on nearly flat faults. Kopeh-Dagh
183 range in northeast accommodates the Arabia-Eurasia convergence through N-S shortening on major
184 thrust faults in the south.

185 3 Modeling

186 3.1 Equations

187 To model the ~~present-day~~ stresses causing deformation in the Zagros-Iranian plateau due to the Arabia-
188 Eurasia collision, we solve ~~three-dimensional (3D)~~ ~~the~~ force balance equations, considering the thin

189 sheet approximation.

$$\frac{\partial \sigma_{ij}}{\partial x_j} + \rho g_i = 0 \quad (1)$$

191 Here σ_{ij} , x_j , ρ , and g_i indicate the ij^{th} component of the total stress tensor, j^{th} coordinate axis, density
192 and acceleration due to gravity respectively (England & Molnar, 1997; Ghosh et al., 2013b).

193 In the above equation, total stress, σ_{ij} is substituted by deviatoric stress using the following relation:

$$\tau_{ij} = \sigma_{ij} - \frac{1}{3} \sigma_{kk} \delta_{ij} \quad (2)$$

195 In the above equation, the Kronecker delta and mean stress are denoted by δ_{ij} and $\frac{1}{3} \sigma_{kk}$ respectively. The
196 force balance equation (1) is integrated up to the base of lithospheric sheet (L), resulting in following
197 full horizontal force balance equations:

$$\frac{\partial \bar{\tau}_{xx}}{\partial x} - \frac{\partial \bar{\tau}_{zz}}{\partial x} + \frac{\partial \bar{\tau}_{xy}}{\partial y} = -\frac{\partial \bar{\sigma}_{zz}}{\partial x} + \tau_{xz}(L) \quad (3)$$

$$\frac{\partial \bar{\tau}_{yx}}{\partial x} + \frac{\partial \bar{\tau}_{yy}}{\partial y} - \frac{\partial \bar{\tau}_{zz}}{\partial y} = -\frac{\partial \bar{\sigma}_{zz}}{\partial y} + \tau_{yz}(L) \quad (4)$$

200 In equation (3) and (4), the over bars indicate integration over depth. Both equations (3 and 4) contain
201 the first term representing horizontal gradients of GPE per unit area ~~in~~~~on~~ the right hand side. On the
202 other hand, the shear tractions at the lithosphere base (L) arising due to mantle convection are denoted
203 by $\tau_{xz}(L)$ and $\tau_{yz}(L)$ (Ghosh et al., 2009).

204 Both of the force balance equations (3 & 4) were solved using ~~the~~ finite element technique (Flesch
205 et al., 2001; Ghosh et al., 2009, 2013b; Singh & Ghosh, 2019, 2020) ~~for a 100 km thick lithosphere of~~
206 ~~varying strength (Figure S1a). The laterally varying viscosities for the lithosphere were assigned from~~
207 ~~Singh & Ghosh (2020)~~. After solving these equations, we obtained the horizontal deviatoric stresses,
208 S_{Hmax} , strain rates as well as plate velocities and compared them with observations.

209 The quantitative comparison between predicted and observed S_{Hmax} axes (Figure 3a) was performed
210 by computing the misfit given by $\sin\theta(1 + R)$ (Ghosh et al., 2013a; Singh & Ghosh, 2019, 2020), where
211 R represents the quantitative difference between stress regimes of observed and predicted S_{Hmax} , while
212 θ denotes the angular difference between both. Hence, this misfit accounts for both the angular and
213 regime misfits with values lying between 0 and 3.

214 The correlation between predicted deviatoric stresses and GSRM strain rates (Figure 3b) (Flesch
215 et al., 2007; Ghosh et al., 2013b; Singh & Ghosh, 2019, 2020) is given by following equation:

$$-1 \leq \sum_{areas} (\varepsilon \cdot \tau) \Delta S / \left(\sqrt{\sum_{areas} (E^2) \Delta S} * \sqrt{\sum_{areas} (T^2) \Delta S} \right) \leq 1 \quad (5)$$

217 where $E = \sqrt{\dot{\varepsilon}_{\phi\phi}^2 + \dot{\varepsilon}_{\theta\theta}^2 + \dot{\varepsilon}_{rr}^2 + \dot{\varepsilon}_{\phi\theta}^2 + \dot{\varepsilon}_{\theta\phi}^2} = \sqrt{2\dot{\varepsilon}_{\phi\phi}^2 + 2\dot{\varepsilon}_{\phi\phi}\dot{\varepsilon}_{\theta\theta} + 2\dot{\varepsilon}_{\theta\theta}^2 + 2\dot{\varepsilon}_{\phi\theta}^2}$, $T = \sqrt{\tau_{\phi\phi}^2 + \tau_{\theta\theta}^2 + \tau_{rr}^2 + \tau_{\phi\theta}^2 + \tau_{\theta\phi}^2} = \sqrt{2\tau_{\phi\phi}^2 + 2\tau_{\phi\phi}\tau_{\theta\theta} + 2\tau_{\theta\theta}^2 + 2\tau_{\phi\theta}^2}$, and $\varepsilon \cdot \tau = 2\dot{\varepsilon}_{\phi\phi}\tau_{\phi\phi} + \dot{\varepsilon}_{\phi\phi}\tau_{\theta\theta} + \dot{\varepsilon}_{\theta\theta}\tau_{\phi\phi} + 2\dot{\varepsilon}_{\theta\theta}\tau_{\theta\theta} + 2\dot{\varepsilon}_{\phi\theta}\tau_{\phi\theta}$. In the above
 218 equation, the second invariants of the strain rate and stress tensors are denoted by E and T . GSRM strain
 219 rates, area and predicted deviatoric stresses are represented by $\dot{\varepsilon}_{ij}$, ΔS , and τ_{ij} respectively. To constrain
 220 the plate velocities, we compute RMS as well as angular misfit between observed and predicted plate
 221 velocities. We also get the relative plate velocities and strain rates as output from models. However, to
 222 calculate the absolute plate velocities and strain rates, we require absolute viscosity values. We compute
 223 the scaling factor for relative viscosities by placing the predicted velocities in a no-net-rotation (NNR)
 224 frame, such that $\int(v \times r) dS = 0$ and minimizing the misfit between the predicted dynamic velocities and
 225 those from Kreemer et al. (2014). Here v denotes the horizontal surface velocity at position r and S is
 226 the area over the Earth's surface (see Ghosh et al. (2013b) for details).
 227

228 3.2 Crustal Models

229 In the right hand side of equations (3 & 4), the first term represents the vertically integrated vertical
 230 stress. It is computed and integrated from the top of variable topography up to depth L (100 km)
 231 (England & Molnar, 1997; Flesch et al., 2001; Ghosh et al., 2013b; Singh & Ghosh, 2019, 2020) using
 232 the following relation:

$$233 \quad \bar{\sigma}_{zz} = - \int_{-h}^L \left[\int_{-h}^z \rho(z') g dz' \right] dz = - \int_{-h}^L (L-z) \rho(z) g dz \quad (6)$$

234 where $\rho(z)$, L and h denote density, the depth to the lithosphere base (100 km) and topographic elevation
 235 respectively. z & z' are variables of integration and g represents the acceleration due to gravity. We also
 236 calculated the stresses for thicker lithosphere ($L=150$ km and $L=200$ km) as studies have shown a much
 237 thicker lithosphere in the region (Robert et al., 2017; Tunini et al., 2017) (Figure S2).

238 The right hand side of equation 6 is given by the negative of GPE per unit area. To calculate GPE
 239 and the stresses associated with it, we used three global crustal models, CRUST2.0 (Bassin et al., 2000),
 240 CRUST1.0 (Laske et al., 2013), and LITHO1.0 (Pasyanos et al., 2014). The upper crust thickness lies
 241 within 15-20 km in the Zagros-Iran region for CRUST2 model (Figure 2a). However, the thickness of the
 242 upper crust in the Zagros-Iranian region is much higher for CRUST1 and LITHO1 (> 25 km) (Figures
 243 2b & c). The Zagros-Iran region has a thicker middle crust (> 20 km) in the case of both CRUST2 and
 244 LITHO1 models (Figures 2d & f), while CRUST1 shows a much thinner middle crust (< 12 km) in this
 245 region (Figure 2e). The lower crust in the Zagros-Iran region is found to be very thin (< 10 km) for all
 246 three models (Figure 2g-i).

247 The density variations in the study area are minimal for CRUST2 model. CRUST2 also shows

248 the highest average density in all three layers ($>2.7 \text{ g/cm}^3$) (Figure 2j,m,p). CRUST1 also indicates
249 an average density of $\sim 2.72 \text{ g/cm}^3$ in the Zagros-Iran region for the upper crust (Figure 2k). The
250 middle and lower crustal layers of CRUST1 show average densities of 2.80 g/cm^3 and $\sim 2.85 \text{ g/cm}^3$,
251 respectively (Figure 2n,q). LITHO1 model shows the lowest average density in the study area for all
252 three layers (Figure 2l,o,r). The upper crust of LITHO models shows an average density of ~ 2.65
253 g/cm^3 . Central Iran block has relatively denser upper crust ($\sim 2.75 \text{ g/cm}^3$), while the density decreases
254 to ~ 2.62 - 2.64 g/cm^3 near the Zagros region. Similar patterns of density variations are observed in the
255 middle and lower crust of LITHO1 model ((Figure 2o,r). Such differences in thickness and density data
256 lead to varying GPE values, and hence subsequently, different stresses.

257 3.3 Mantle Convection

258 We ran mantle convection models using HC (Hager & O'Connell, 1981). HC is a semi-analytical mantle
259 convection code that uses density anomalies derived from seismic tomography models and radial vis-
260 cosity as inputs. Here, we considered four global mantle convection models, S40RTS (Ritsema et al.,
261 2011), SAW642AN (Mégnin & Romanowicz, 2000), 3D2018_S40RTS and S2.9_S362 to infer the man-
262 tle density anomalies. 3D2018_S40RTS is a merged model of SV wave upper mantle tomography model,
263 3D2018_Sv given by Debayle et al. (2016), and S40RTS. S2.9 is a global tomography model of the up-
264 per mantle with higher resolution which is given by Kustowski et al. (2008b). We merged this model
265 with the global shear wave velocity model, S362ANI (Kustowski et al., 2008a) to obtain the merged
266 tomography model of S2.9_S362. **We used two different radial viscosity structures, namely GHW13**
267 **which is the best viscosity model from Ghosh et al. (2013b), and SH08 given by Steinberger & Holme**
268 **(2008). GHW13 is a four layered viscosity structure, with a highly viscous lithosphere ($\sim 10^{23} \text{ Pa-s}$).**
269 **The viscosity drops to $\sim 10^{20} \text{ Pa-s}$ in the asthenosphere, which again increases to $\sim 10^{21} \text{ Pa-s}$ in upper**
270 **mantle and $\sim 10^{22} \text{ Pa-s}$ in the lower mantle (Figure S1b). On the other hand, the viscosity in SH08**
271 **model increases gradually with depth and it has a slightly weaker lithosphere as compared to GHW13.**
272 **It has the highest viscosity value of 10^{23} Pa-s around 2000-2300 km depth, and significantly lower vis-**
273 **cosity for D'' layer (Figure S1b). GHW13 viscosity model performed slightly better than SH08 in fitting**
274 **the observed parameter, thus we have shown results from the same throughout this paper. However, we**
275 **have also included the the predicted results and their fit to the observables in the supplementary section**
276 **(Table S1). The radial viscosity model from Ghosh et al. (2013b), was used in our study to run mantle**
277 **convection models.**

278 **3.4 Data**

279 To have better constraints on our **this study's** models, we also estimated S_{Hmax} (most compressive hor-
280 izontal principal axes) orientations as well as plate velocities. Various deformation indicators such as
281 S_{Hmax} orientations from the World Stress Map (WSM) (Heidbach et al., 2016), strain rates and plate
282 velocities from Global Strain Rate Model (Kreemer et al., 2014) were used to perform a quantitative
283 comparison with our the predicted results of **this study** (Figure 3).

284 WSM data is a global database of the crustal stress field obtained from various sources such as focal
285 mechanisms; geophysical logs of borehole breakouts and drilled induced fractures; engineering methods
286 such as hydraulic fractures and overcoring; and geological indicators that are obtained from fault slip
287 analysis and volcanic alignments. These data have been assigned quality ranks from A to E based on
288 the accuracy range. A-type data suggests that the standard deviations of S_{Hmax} orientations are within
289 $\pm 15^\circ$ range, $\pm 20^\circ$ for B-type, $\pm 25^\circ$ for C-type and $\pm 40^\circ$ for D-type. However, E-type indicates the
290 data records are either incomplete or from non-reliable sources or the accuracy is $> \pm 40^\circ$. Our **This**
291 study uses A-C quality stress data records (Figure 3a). Observed S_{Hmax} axes are aligned in NNE-SSW
292 directions in Zagros with dominant thrust faulting. NW and Central Iran show some strike-slip mode of
293 deformation with NE-SW compressional directions.

294 The strain rates and plate velocities are taken from GSRM v2.1 model (Kreemer et al., 2014) (Figure
295 3b). GSRM v2.1 provides a global data set of strain rates and plate motions that are determined using
296 $\sim 22,500$ geodetic plate velocities. Higher strain rates are observed along the simply folded mountains
297 ($\sim 40 - 100 \times 10^{-9}/\text{yr}$). Most of Iran shows strain rates in between $4 - 10 \times 10^{-9}/\text{yr}$. The plate motions
298 used in our study for comparing with predicted velocities are given in a no-net-rotation (NNR) frame
299 interpolated on a $1^\circ \times 1^\circ$ grid. The velocity vectors show an eastward motion in the study area, which
300 becomes nearly E-W in Afghan Block (Figure 3b).

301 **4 Results**

302 **4.1 Stress and deformation due to GPE**

303 Three crustal models (CRUST1.0, CRUST2.0 and LITHO1.0) were used to compute GPE within the
304 study region. The second invariant of stress computed using GPE lies within $\sim 10-12$ MPa along the
305 Zagros for CRUST2 and CRUST1 models (Figure 4a,c). LITHO1 model predicts larger stress magni-
306 tudes along Zagros (Figure 4e). NE-SW compressional stresses are observed along the frontal faults of
307 Zagros (MFF) (Figure 1a,c). The central part of Zagros thrust faults (MZT) shows the strike-slip mode
308 of faulting for nearly all three models (Figures 4 & 4b,d & f). The strike-slip regime further extends

309 into Sanandaj-Sirjan Zone (SSZ) while lies north of MZT for CRUST2 and LITHO1 model (Figure
310 4b,f), while it transitions to thrust type of deformation in the north of MZT for CRUST1 (Figure 4d).
311 The Urmia-Dokhtar Magmatic Arc (UDMA) and central Iran also show the strike-slip mode of fault-
312 ing for CRUST2 and LITHO1. The north of MRF shows tension for CRUST2 model, while CRUST1
313 predicts this area to be predominantly strike-slip. On the other hand, the entire region shows significant
314 compression for LITHO1 model.

315 We compared predicted S_{Hmax} from our three GPE only models to observed S_{Hmax} orientations and
316 type obtained from WSM (Heidbach et al., 2016) by computing Regime misfit (Figure 5, left panel).
317 The average misfit is lowest for LITHO1 model with a value of 0.59 (Figure 5g), while CRUST2 model
318 shows the highest average misfit of 0.77 (Figure 5a). High misfits (2 – 3) are observed North of MRF
319 and Tehran for CRUST2, while lowest (< 1) in case of LITHO1, suggesting that the dominant mode
320 of faulting in this area is possibly thrust as opposed to normal deformation predicted by CRUST2. In
321 central Iran, S_{Hmax} misfit is low (< 1) when the dominant mode of deformation is strike-slip as predicted
322 LITHO1 model.

323 On calculating the correlation between the predicted deviatoric stresses and GSRM strain rates, the
324 LITHO1 model shows the highest average correlation (0.92) (Figure 5, middle panel). The correlation
325 is found to be extremely poor (~ -1) for CRUST2 model in the north of MRF (Figure 5b). Such
326 poor correlation suggests that the predicted stresses differ entirely from those causing deformation. For
327 example, anti-correlation in north of MRF suggests that the dominant mode of deformation in this area
328 might be thrust rather than normal faulting. Again, the correlation coefficient is less than 0.2 in the
329 central Iranian Block for CRUST2 and CRUST1 models (Figure 5b,e), while LITHO1 model shows a
330 better correlation suggesting the strike-slip type of deformation to be more prominent in central Iran
331 (Figure 5h).

332 We predicted the plate velocities for all three models in the NNR frame and compared them with
333 observed plate velocities obtained from Kreemer et al. (2014) (Figure 5 right panel). CRUST2 gives
334 the least RMS error (7.32 mm/yr) and the lowest angular misfit (5.5°) (Figure 5c). LITHO1 model
335 shows high misfits ($> 20^\circ$) between observed and predicted velocities in the east of the central Iran (i.e.
336 Afghan Block) (Figure 5i). Both CRUST2 and LITHO1 models predict the plate velocities very close to
337 observed ones in the Zagros mountains, as shown by nearly zero angular misfits along Zagros (Figures
338 5c & i). CRUST1 performs average in predicting the plate velocities in the study area (Figure 5f).

339 Interestingly, the use of thicker lithosphere to calculate GPE leads to the introduction of more com-
340 pressional stresses in the region (Figure S2a-f). The average misfit between predicted and observed
341 S_{Hmax} is found to be lowest for the 200 km thick lithosphere (Table S2). Similarly, the correlation be-
342 between strain rate tensor and predicted stresses,; and rms error between observed and predicted NNR

343 velocities show significant improvement for thicker lithosphere. However, the improvement in fit is bet-
344 ter for CRUST2 as opposed to the other two models, CRUST1 and LITHO1, where the misfit between
345 observed and predicted velocities show an increase. Thus, we can say that while considering lithospheric
346 contributions only, the thicker lithosphere does a better job of explaining the observed deformation in-
347 dicators (Table S2).

348 4.2 Stress and deformation due to Mantle Convection

349 The deviatoric stresses predicted using all four mantle convection models are found to be mostly com-
350 pressional along MFF (Figure 6). All models, except for SAW642AN, predict the strike-slip mode of
351 faulting in NW parts of Zagros with nearly E-W oriented extensional axes and N-S compressional axes
352 (Figures 6a,e & g). On the other hand, SAW642AN shows predominant compression within this area
353 (Figure 6e). S40RTS, 3D2018_Sv, and S2.9_S362 show strike-slip deformation in NW parts of SSZ,
354 UDMA and NW Iran. Central Iran is predicted to have mostly compressional stresses by all models
355 except for S40RTS. Thrust type of deformation is predicted in Afghan Block by all models with some
356 intermittent strike-slip deformation. SINGH_SAW model predicts the whole Afghan Block in the strike-
357 slip regime (Figure 6g-h). S40RTS and S2.9_S362 predict higher stress magnitude in NW parts of the
358 Zagros Orogeny system and Central Iran compared to other models.

359 The misfit between observed and predicted S_{Hmax} is found to be much lower for mantle convection
360 models (0.54-0.57) (Figure 7 left panel), than those of GPE only models (Figure 5 left panel), evidently
361 showing the importance of mantle flow. The lowest average misfit is observed for SAW642AN (0.54)
362 (Figure 7d). Though the misfit increases in the east, Lut block, and near MSZ. The correlation of
363 predicted deviatoric stresses with GSRM strain rates improves over GPE only models (Figure 7 middle
364 panel), with SAW642AN yielding the highest correlation coefficient (0.91) (Figure 7e). Correlation
365 drops below 0.4 parts of central Iran. S40RTS performs predicts the plate velocities closest to the
366 observed one, out of all models, with the least RMS error (6.20 mm/yr) between predicted and observed
367 plate velocities (Figure 7c). On the other hand, SAW642AN and 3D2018_S40RTS models show high
368 misfits (rms error ~ 10 mm/yr), as they are unable to match observed plate velocities in Zagros-Iran
369 plateau, both in orientations and magnitude (Figures 7f & i).

370 As discussed above, mantle convection models perform better in predicting deviatoric stresses in the
371 study area **which is evident by high correlation between predicted stresses and observed strain rates; and**
372 **low misfits between observed and predicted S_{Hmax}** . However, the error in predicting plate velocities is
373 higher for mantle convection models than in GPE only models. **GPE only models perform slightly better**
374 **in predicting the orientation and magnitude of velocity vectors.** Thus, **As there are still significant misfits**
375 **in fitting the observables,** we added the deviatoric stresses predicted from GPE differences and Mantle

376 convection models to constrain the **total** stress field in the Zagros-Iranian plateau that may account for
377 both forces.

378 We also ran S40RTS model with LAB (Lithosphere-Asthenosphere boundary) at 150 and 200 km
379 (Figure S2g-h). Similar to GPE models, the fit to observed data shows an improvement when LAB is at
380 200 km, though the stress patterns do not change significantly (Table S2).

381 **4.3 Stress and deformation by GPE and Mantle convection**

382 Adding mantle contributions to GPE only models led to significant changes in total deviatoric stresses
383 for all models (Figure 8,9,10). There is a significant increase in total stress magnitude of the entire study
384 area; except for north of MRF and SE of central Iran, which show slightly lower stresses (< 16 MPa)
385 for combined models of CRUST2 and mantle convection (Figure 8). These models show predominant
386 compression in most of Zagros, SSZ, UDMA, NW and central Iran, except for the strike-slip type of
387 deformation in NW parts. The joint models of CRUST1 and mantle convection predict higher stresses
388 (> 25 MPa) in NW Iran and at MFF (Figure 9). Interestingly, the stresses drop below 20 MPa towards
389 the north of HZF, MRF till the south Capsian. The combined models of CRUST1 and mantle convection
390 show compressional stresses are dominant in the study area, with occasional strike-slip faulting in the
391 north-west (Figure 9 right panel). The stresses predicted by combined models of LITHO1 and mantle
392 convection models are higher in magnitude than other models in the study area (> 25 MPa) (Figure 10).
393 S40RTS+litho and S2.9_S362+litho models show high stresses in Zagros (>50 MPa)(Figure 10a,g).

394 The combined models show a lower misfit between observed and predicted S_{Hmax} (Figure 11), espe-
395 cially when compared to GPE only models (Figure 5 left panel). SAW642AN+litho showed the lowest
396 average misfit of 0.47 (Figure 11f). Interestingly, SAW642ANcr2 and 3D2018_S40RTScri2 show low
397 misfits in the Zagros-Iranian plateau region, despite not having the lowest average misfit (Figures 11d
398 & g). The higher misfits in NW Iran and SE of the central Iran block observed for GPE only models
399 get reduced significantly due to the addition of mantle derived stresses, referring to the importance of
400 mantle convection in these areas.

401 As we look at the correlation between predicted stress tensors and GSRM strain rate tensors, the over-
402 all correlation is better for combined models (Figure 12), especially for combined models of LITHO1
403 and mantle convection (Figure 12 right panel). A high average correlation coefficient of 0.94 is ob-
404 served for SAW642AN+litho, 3D2018_S40RTS+litho as well as S2.9_S362+LITHO1 (Figures 12f, i &
405 l). Despite an overall improvement in correlation between observed strain tensors and predicted devia-
406 toric stresses, the correlation is found to be much poor in areas such as NW parts of Zagros and east of
407 central Iranian block, for combined models of mantle convection and GPE only models of CRUST2 &
408 CRUST1 (Figure 12 left and middle panels). In NW Zagros, mantle only models are found to perform

409 much better, as they show better correlation (Figure 7 middle panel), thus suggesting mantle derived
410 stresses are needed to be much higher than those from GPE to explain the observed deformation in these
411 areas.

412 Again the combined models of GPE and mantle tractions give lower rms errors, when predicted
413 plate velocities are compared to the observed ones. S40RTScr2 shows the least rms error (3.28 mm/yr)
414 and the least average angular misfit (3.0°) between predicted and observed plate velocities (Figure 13a).
415 Relatively the combined models of S40RTS/S2.9_S362 and GPE perform much better than other models
416 in predicting the orientation and magnitudes of plate velocities. Significant misfits are observed for
417 SAW642ANcr1 and 3D2018_S40RTScr1 models. **The joint models of S40RTS and GPE for thicker**
418 **lithosphere do not offer any significant changes in stresses and their fit to observed data (Table S2)**
419 **(Ghosh et al., 2009; Jay et al., 2018; Hirschberg et al., 2018).** Thus, considering the lithosphere base at
420 100 km appears to be a satisfactory approach.

421 5 Discussion

422 The Zagros-Iranian plateau region is formed due to the convergence of Arabian plate towards **the** Eur-
423 **asian plate.** Zagros mountain belt demarcates the southwestern boundary of the deformation zone,
424 whereas, it is bounded by the Makran subduction zone in the southeast and by Afghan Block in the
425 east. Kopet-Dagh and Arborz act as this region's northeastern and northern boundaries (Irandoost et al.,
426 2022). We modeled the stresses and deformation parameters in the study area by solving the force bal-
427 ance equation using the finite element method for a global grid of $1^\circ \times 1^\circ$ resolutions, considering two
428 primary sources of stresses; GPE and mantle tractions. GPE was calculated using the thickness and den-
429 sity variation from the different global models like CRUST1.0, CRUST2.0 and **LITHO1.0**. The shear
430 tractions were computed from density derived mantle convection model.

431 The magnitude of stresses due to GPE variations was below 15 MPa in the Iranian plateau for
432 CRUST2 and CRUST1 models (Figures 4a & c). However, **LITHO1** model predicted higher stresses
433 (> 30 MPa) with predominant compression in parts of the Zagros-Iran region and Afghan block. Most of
434 the convergence of Arabian and Eurasian plates has been accommodated through shortening across Za-
435 gros (Irandoost et al., 2022; Khodaverdian et al., 2015). Walpersdorf et al. (2006); Hessami et al. (2006)
436 suggested nearly pure N-S shortening of 8 ± 2 mm/yr in southeastern Zagros. The convergence occurs
437 perpendicular to the simply folded mountains and is restricted to the shore of Persian Gulf. Earthquake
438 focal mechanisms also show reverse faulting within this area (Berberian, 1995; Hatzfeld et al., 2010;
439 Hatzfeld & Molnar, 2010; Irandoost et al., 2022). In our study, **LITHO1** model predicted thrust mode
440 of faulting within Zagros, which is consistent with these results. In NW Zagros, Hatzfeld et al. (2010);

441 Hatzfeld & Molnar (2010); Jackson & McKenzie (1984); Khorrami et al. (2019); Talebian & Jackson
442 (2002) and various others have suggested partitioning of deformation. The oblique shortening is par-
443 titioned into strike-slip faulting that is accommodated by MRF, while shortening occurs perpendicular
444 to the the mountain belt (Hatzfeld et al., 2010; Hatzfeld & Molnar, 2010; Jackson & McKenzie, 1984;
445 Khorrami et al., 2019; Talebian & Jackson, 2002). On considering lithospheric models only, we pre-
446 dicted the normal mode of faulting to be dominant in this area for CRUST2. On the other hand, CRUST1
447 model predicted strike-slip components in the northern segment of MRF, while LITHO1 showed thrust
448 type of deformation in this area. Interestingly, the misfits of predicted parameters with various observa-
449 tions of S_{Hmax} , strain rates and plate velocities were found to be lowest for LITHO1 model, thus arguing
450 for thrust type of deformation in this area. SSZ in north of MZT consists of various thrust systems
451 (Alavi, 1994). CRUST1 predicted thrust mode of faulting in this region, while CRUST2 and LITHO1
452 models showed intermittent strike-slip type of faulting. Alborz as well as Kopeh Dagh in the north
453 has also been subjected to reverse faulting (Allen et al., 2003; Hatzfeld & Molnar, 2010; Hollingsworth
454 et al., 2010; Irandoost et al., 2022; Khodaverdian et al., 2015), which has also been shown by CRUST1
455 and LITHO1 models. Models predicting thrust in Talesh mountains show low misfits to observation
456 suggesting thrusting of the mountain range over the basin with slip vectors directed towards the South
457 Caspian Sea (Irandoost et al., 2022). The N-S convergence in Kopeh-Dagh range iswas predicted by
458 LITHO1 model considering the contribution from lithospheric density and topographic variations only.
459 The shearing between Central Iran and Afghan Block caused due to varying rates of shortening across
460 the Zagros, Alborz and Caucasus, is accommodated by strike-slip faults near Lut block boundaries
461 (Khorrami et al., 2019; Vernant et al., 2004; Walpersdorf et al., 2014). Again, LITHO1 model predicted
462 similar strike-slip deformation in these areas; however, CRUST2 and CRUST1 failed to do so.

463 The stresses predicted using basal tractions were mostly compressional in southeastern Zagros owing
464 to the convergence of Arabia-Eurasia (Figure 6). However, all models, except SAW642AN predicted
465 strike-slip type of deformation in the northwestern Zagros (MRF), which concurs with the results from
466 various studies (Hatzfeld et al., 2010; Hatzfeld & Molnar, 2010; Jackson & McKenzie, 1984; Khorrami
467 et al., 2019; Talebian & Jackson, 2002). The mantle derived stress parameters showed a better fit to
468 observables than those from GPE variations (Figures 7 left and middle panel), though the correlation
469 dropped below 0.5 in Central Iran. Here, mantle convection models foundpredicted compressional type
470 of deformation, while Baniadam et al. (2019); Khorrami et al. (2019) suggested that strike-slip faulting
471 along the fault system bounding Lut Block. The velocity misfits were very high for all models except
472 S40RTS (Figure 7 right panel). Although we used four tomography models to compute the mantle-
473 derived stresses, the stress regimes for all models are found to be similar, with varying magnitudes. Such
474 results suggest that nearly all four seismic tomography models are relatively consistent in predicting the

475 stresses in this region.

476 Adding the GPE derived stresses to those from the mantle to obtain the total lithospheric stress field
477 showed a notable improvement in constraining the observed deformation parameters. The final stress
478 regimes also varied significantly depending on particular combinations of GPE and mantle convection
479 models. All joint models of CRUST2 and mantle tractions showed lower magnitudes of stresses (< 15
480 MPa) in the north of MRF, Tehran and southern Lut block. The stresses showed an obvious increase
481 in these areas for other models. Significantly higher stresses (> 30 MPa) were also observed near the
482 collisional front (MFF) for all models. On comparing with observations, combined models of CRUST2
483 and mantle tractions showed significant improvement in fit, except in areas north of MRF and Tehran.
484 CRUST1 model when added with mantle contribution, predicted thrust faulting along the faults bound-
485 ing Lut Block, leading to poor correlation (< 0.5). On the other hand, combined LITHO1 and mantle
486 convection models gave a much better fit in this area, as they predicted strike-slip faulting. The use of
487 different mantle convection models is much less sensitive in the Iran-Zagros region, as most models can
488 match various surface observables reasonably well.

489 On running various models and comparing the stresses in Zagros-Iran, we try to explain the relative
490 roles of GPE and mantle tractions in causing observed deformation. The contributions from both sources
491 vary significantly among different models. However, these variations arise mainly from GPE only mod-
492 els, which may be due to uncertainties in crustal models of this area. Another interesting observation
493 from this study is that the role of GPE in the study region may not be that significant, as mantle derived
494 stresses were able to explain many of the deformation indicators. To get a quantitative constraint on the
495 best model, we computed a total error as given below:

$$Total\ error = S_{Hmax}\ error + 1 - C_{strain} + V_{rms} \quad (7)$$

496 S_{Hmax} error in the above equation is calculated as mentioned in section 3.4, while C_{strain} is the
497 correlation computed using equation 6. V_{rms} is the rms error between predicted and observed velocities.
498 The total errors calculated using equation 7 have been tabulated in Table 1. S40RTScr2 is found to have
499 the lowest error.

500 We also calculated plate velocities with respect to the Eurasian plate (Figure 14) and compared them
501 with observed GPS velocities relative to Eurasia. The GPS velocities were obtained from various studies
502 conducted in the study [this](#) area (ArRajehi et al., 2010; Bayer et al., 2006; Frohling & Szeliga, 2016;
503 Khorrami et al., 2019; Masson et al., 2006, 2007; Raeesi et al., 2017; Reilinger & McClusky, 2011;
504 Vernant et al., 2004). GPS measurements show a northward convergence rate of $\sim 22\text{mm/yr}$ for Arabia
505 relative to Eurasia (Reilinger et al., 2006; Vernant et al., 2004), however, it varies significantly along
506 the Zagros. The southeastern Zagros show the highest convergence rates of $\sim 25\text{ mm/yr}$ oriented in

Table 1: Summary of quantitative comparison of predicted results of various models with observed data.

Model	S_{Hmax} misfit	Strain rate correlation	RMS error (mm/yr)	Angular misfit	Total error
CRUST2	0.77	0.69	7.32	5.5	3.07
CRUST1	0.64	0.87	7.44	8	2.78
LITHO1	0.59	0.92	8.51	9	2.81
S40RTS	0.57	0.88	6.2	4.6	2.51
SAW642AN	0.54	0.91	11.35	13	3.06
3D2018_S40RTS	0.56	0.88	9.44	9.7	2.92
S2.9_S362	0.57	0.88	8.29	9	2.81
S40RTS _{cr2}	0.48	0.92	3.28	3	1.75
SAW642AN _{cr2}	0.49	0.92	4.77	5.5	2.13
3D2018_S40RTS _{cr2}	0.49	0.91	4.06	4.5	1.98
S2.9_S362 _{cr2}	0.48	0.92	4.24	5.1	2.00
S40RTS _{cr1}	0.51	0.92	4.29	5.5	2.05
SAW642AN _{cr1}	0.5	0.92	7.39	9.6	2.58
3D2018_S40RTS _{cr1}	0.51	0.91	6.35	8.2	2.45
S2.9_S362 _{cr1}	0.51	0.92	4.78	6.6	2.15
S40RTS+litho1	0.49	0.93	4.52	6.1	2.07
SAW642AN+litho1	0.47	0.94	6.42	7.4	2.39
3D2018_S40RTS+litho1	0.48	0.94	5.62	7.2	2.27
S2.9_S362+litho1	0.48	0.94	5.8	8.3	2.30

507 north-northeast directions. GPS vectors are oriented northward in Central Zagros, which transitions
 508 north-northwest in NW parts of Zagros with the lowest convergence rates of ~ 18 mm/yr (Hatzfeld &
 509 Molnar, 2010; Hatzfeld et al., 2010; Khorrami et al., 2019). Vernant et al. (2004) suggested that MSZ
 510 accommodates most of the shortening (19.5 ± 2 mm/yr) in the east of $58^\circ E$, while fold and thrust belts of
 511 Zagros, Alborz and Caucasus collectively accommodate the shortening in west of $58^\circ E$. GPS velocities
 512 in the east of Iran (Afghan Block) are very small in magnitude. To the west, velocities increase showing
 513 westward rotation of Antolia (Khorrami et al., 2019; Reilinger et al., 2006). The northern part of Iran
 514 shows that GPS vectors are aligned towards the northeast. We found that the combined model of S40RTS
 515 and CRUST2 can approximately match the GPS velocities (Figure 14a). Predicted plate velocities with
 516 respect to the fixed Eurasian plate show a northward movement of 2-3 cm/yr in southeastern Zagros.
 517 The plate moves in NNE direction east of central Zagros ($53^\circ E$). On the other hand, west of $53^\circ E$
 518 shows a movement in NNW direction, becoming much more prominent in the north. However, the
 519 convergence rates in the east of Iran i.e. Lut Block as well as Afghan Block, is predicted to be much
 520 higher ($\sim 1 - 2$ cm/yr) than those suggested by various observations. Plate velocities predicted by joint
 521 models, S40RTS_{cr1} and S40RTS+LITHO1 show nearly N-S contraction of very high magnitudes
 522 (4-5 cm/yr) throughout the region (Figure S3), which suggests much higher rates of deformation than
 523 those suggested by above-mentioned studies.

524 We also used shear wave splitting measurements to further study the deformation in the Zagros-Iran

525 region by comparing them with S_{Hmax} (Figure 14b). The fast polarization directions (FPDs) are the in-
526 dicators of seismic anisotropy. We consider two primary causes of seismic anisotropy; induced by stress
527 and due to structure of the region (Yang et al., 2018). If the FPDs are parallel to S_{Hmax} orientations, it
528 suggests that anisotropy is associated with stress. On the other hand, latter kind of anisotropy is related
529 with the alignment of fault, fast axes of minerals that may cause polarization, and sedimentary bedding
530 planes. The FPDs in our study were obtained from Sadeghi-Bagherabadi et al. (2018); Kaviani et al.
531 (2009, 2021). The FPDs are subparallel to S_{Hmax} orientations in NW Zagros, Arabian plate, northern
532 Iran and MSZ. Such a correlation between both indicates that anisotropy in this region may be stress
533 induced. **Additionally, the correlation of S_{Hmax} orientations and FPDs argues for a good coupling be-**
534 **tween lithosphere and mantle in those areas. In contrast, Sadeghi-Bagherabadi et al. (2018) showed**
535 **FPDs parallel to the strike of the fault (sub-parallel to S_{Hmax} directions of CRUST2), In NW Zagros,**
536 **Sadeghi-Bagherabadi et al. (2018) also showed FPDs parallel to the strike of the fault, suggesting seis-**
537 **mic anisotropy mainly reflects the deformation in the lithospheric mantle. Again, FPDs are subparallel**
538 **to the strike of range in northeastern Iran, eastern Kopeh Dagh and central Alborz indicating structure-**
539 **induced anisotropy caused by strong shearing along the strike-slip faults (Gao et al., 2022; Kaviani et al.,**
540 **2021).**

541 To explore the relative roles of lithospheric and mantle derived stresses, we compared the deviatoric
542 stresses from CRUST2 to those from S40RTS. We performed a correlation between both stresses by
543 using equation 5 and found a high correlation (> 0.5) near MSZ and central Zagros (Figure 14c). The
544 correlation degrades north of the simply folded mountains and NW Iran. The stresses are anti-correlated
545 in northwestern parts of higher Zagros, north of MRF and Tehran, as CRUST2 predicted NNE-SSW
546 tension (Figure 4b) as opposed to the strike-slip faulting predicted by S40RTS (Figure 6b). Lut Block
547 also shows a slight anticorrelation between stresses (~ -0.5), as the stresses predicted by CRUST2
548 are very low. The log of the ratio of second invariants of deviatoric stresses from GPE variations (T_1)
549 to that of mantle tractions (T_2) is plotted in Figure 14d. Positive values of logarithmic ratio suggests
550 the dominance of GPE derived stresses over mantle ones, as observed in the south of the collisional
551 boundary (MFF). The ratio is negative in most parts of the Iranian plateau and Zagros, indicating that
552 the magnitude of mantle derived stresses **is** higher than **that of** those from GPE, especially in higher
553 Zagros and central Iran (Figure 14d).

554 The deformation in the Zagros-Iran plateau region has been found to exhibit various similarities to
555 another similar complex collision zone, i.e. the Himalaya-Tibetan plateau region as both continental
556 collisions went through many of the same processes. The high topography in both collisions reflects
557 ongoing crustal deformation through crustal thickening and shortening. However, there are differences
558 in convergence rates, total amounts of convergence and various stages of development of the Zagros-Iran

559 and Himalaya-Tibet regions (Hatzfeld & Molnar, 2010). Singh & Ghosh (2020) studied the deformation
560 in the Himalaya-Tibet region by joint modeling of lithosphere and mantle. They showed that GPE
561 plays a crucial role in the ongoing deformation of the India-Eurasia collision zone, as it leads to the
562 observed E-W extension in Tibetan plateau. In contrast, we found that GPE has a much lesser role in the
563 Zagros-Iran plateau region (Figure 14d), and no normal mode of faulting is observed in this area. In the
564 Zagros-Iran plateau region, mantle convection appears to be the primary driver of deformation in most
565 parts as discussed above. Despite these differences, numerical models argue for a good coupling between
566 the lithosphere and mantle in both collision zones, which is also supported by seismic anisotropy studies
567 in both regions (Kaviani et al., 2021; Singh et al., 2016; Sol et al., 2007).

568 6 Conclusion

569 The Zagros-Iranian plateau region has large deformations along and across the collision zones. There-
570 fore, we conducted numerical simulation studies for stress and deformations. The stresses predicted
571 in this region were primarily compressional, with magnitudes lower than 30 MPa. The southeastern
572 boundary of Zagros was found to be under high stress which is also reflected by higher convergence
573 rates. Mantle convection models were able to constrain most observations in the Iranian plateau.
574 However, the misfits with observations were much larger in the east of Iran, when only mantle con-
575 tributions were considered. The combined models of lithosphere and mantle-derived stresses can
576 explain surface observables in most of the area, suggesting a good lithosphere-mantle
577 coupling, except for east of Iran. The fit between both predicted and observed data increases after
578 considering mantle derived stresses. The shearing in those areas was predicted by lithospheric models,
579 though variation in lithospheric and density structure given by these models lead to varying degree of
580 misfits. Hence, there is a need for better constraint on lithospheric structure in this area.

581 The mantle derived stresses were found to be much higher than lithospheric stresses, thus the over-
582 all stress regimes predicted by combined models were more biased towards the compressional type of
583 stresses. This caused our combined models to predict thrust mode of faulting in most cases, especially
584 when lithospheric derived stresses were computed from CRUST1 and LITHO1 models. CRUST2 model
585 predicted more extensional stress in the Iranian plateau, which in turn balanced the effect of compres-
586 sional stresses predicted by mantle convection models; hence leading to prominence of strike-slip mode
587 of faulting in the northwestern parts of study region. The rate of convergence of Arabia relative to a
588 fixed Eurasia was found to vary along the Zagros orogeny in a similar way to GPS measurements.

589 **Open Research Section**

590 We used three models, namely CRUST1.0, CRUST2.0, and LITHO1.0, for obtaining the data of crustal
591 and lithospheric structure, which are required as inputs in finite element models. We downloaded these
592 three models and the seismic tomography models used in mantle convection codes from the Incorporated
593 Research Institutions for Seismology (IRIS) Earth Model Collaboration repository (<http://ds.iris.edu/ds/products/emc-earthmodels/>). The strain rate model, GSRMv2.1 was obtained from <http://geodesy.unr.edu/GSRM/>. World Stress Map Website (<https://www.world-stress-map.org/>)
594 provides the $S_{H\max}$ orientations and type of faulting, which were used to perform a quantitative com-
595 parison with predicted results. GPS velocities relative to Eurasia were taken from ArRajehi et al.
596 (2010); Bayer et al. (2006); Frohling & Szeliga (2016); Khorrami et al. (2019); Masson et al. (2006,
597 2007); Raeesi et al. (2017); Reilinger & McClusky (2011); Vernant et al. (2004). We also used seismic
598 anisotropy data from Sadeghi-Bagherabadi et al. (2018); Kaviani et al. (2009, 2021).
599
600

601 **Acknowledgments**

602 We are grateful to Dr. Attreyee Ghosh for sharing the codes for finite element modeling of stresses.
603 We thank the director CSIR-NGRI for permission to publish this work (Ref. No. NGRI/Lib/2022/ Pub-
604 110). This article is published as a part of MLP-FBR-003(AM) Project. The figures of this article are
605 generated from gmt.

606 **References**

607 Agard, P., Omrani, J., Jolivet, L., & Moutherau, F. (2005). Convergence history across Zagros (Iran):
608 constraints from collisional and earlier deformation. *International journal of earth sciences*, 94(3),
609 401–419.

610 Agard, P., Omrani, J., Jolivet, L., Whitechurch, H., Vrielynck, B., Spakman, W., Monié, P., Meyer, B., &
611 Wortel, R. (2011). Zagros orogeny: a subduction-dominated process. *Geological Magazine*, 148(5-6),
612 692–725.

613 Alavi, M. (1980). Tectonostratigraphic evolution of the Zagrosides of Iran. *Geology*, 8(3), 144–149.

614 Alavi, M. (1994). Tectonics of the Zagros orogenic belt of Iran: new data and interpretations. *Tectono-*
615 *physics*, 229(3-4), 211–238.

616 Allen, M., Ghassemi, M., Shahrabi, M., & Qorashi, M. (2003). Accommodation of late Cenozoic oblique
617 shortening in the Alborz range, northern Iran. *Journal of structural geology*, 25(5), 659–672.

618 Allen, M.B. & Armstrong, H.A. (2008). Arabia–Eurasia collision and the forcing of mid-Cenozoic
619 global cooling. *Palaeogeography, Palaeoclimatology, Palaeoecology*, 265(1-2), 52–58.

620 Allen, M.B., Kheirkhah, M., Emami, M.H., & Jones, S.J. (2011). Right-lateral shear across Iran and
621 kinematic change in the Arabia—Eurasia collision zone. *Geophysical Journal International*, 184(2),
622 555–574.

623 ArRajehi, A., McClusky, S., Reilinger, R., Daoud, M., Alchalbi, A., Ergintav, S., Gomez, F., Sholan,
624 J., Bou-Rabee, F., Ogubazghi, G., et al. (2010). Geodetic constraints on present-day motion of the
625 Arabian Plate: Implications for Red Sea and Gulf of Aden rifting. *Tectonics*, 29(3).

626 Austermann, J. & Iaffaldano, G. (2013). The role of the Zagros orogeny in slowing down Arabia-Eurasia
627 convergence since~ 5 Ma. *Tectonics*, 32(3), 351–363.

628 Authemayou, C., Bellier, O., Chardon, D., Malekzade, Z., & Abassi, M. (2005). Role of the Kazerun
629 fault system in active deformation of the Zagros fold-and-thrust belt (Iran). *Comptes Rendus Geo-*
630 *science*, 337(5), 539–545.

631 Ballato, P., Uba, C.E., Landgraf, A., Strecker, M.R., Sudo, M., Stockli, D.F., Friedrich, A., & Tabatabaei,
632 S.H. (2011). Arabia-Eurasia continental collision: Insights from late Tertiary foreland-basin evolution
633 in the Alborz Mountains, northern Iran. *Bulletin*, 123(1-2), 106–131.

634 Baniadam, F., Shabanian, E., & Bellier, O. (2019). The kinematics of the Dasht-e Bayaz earthquake fault
635 during Pliocene-Quaternary: implications for the tectonics of eastern Central Iran. *Tectonophysics*,
636 772, 228218.

637 Bassin, C., Laske, G., & Masters, G. (2000). The current limits of resolution for surface wave tomogra-
638 phy in {North America}. *EOS Trans AGU*, 81.

639 Bayer, R., Chery, J., Tatar, M., Vernant, P., Abbassi, M., Masson, F., Nilforoushan, F., Doerflinger,
640 E., Regard, V., & Bellier, O. (2006). Active deformation in Zagros—Makran transition zone inferred
641 from GPS measurements. *Geophysical Journal International*, 165(1), 373–381.

642 Berberian, M. (1995). Master “blind” thrust faults hidden under the Zagros folds: active basement tec-
643 tonics and surface morphotectonics. *Tectonophysics*, 241(3-4), 193–224.

644 Berberian, M. & King, G. (1981). Towards a paleogeography and tectonic evolution of Iran. *Canadian*
645 *journal of earth sciences*, 18(2), 210–265.

646 Bird, P. (1998). Testing hypotheses on plate-driving mechanisms with global lithosphere models includ-
647 ing topography, thermal structure, and faults. *Journal of Geophysical Research: Solid Earth*, 103(B5),
648 10115–10129.

649 Coblenz, D., Richardson, R.M., & Sandiford, M. (1994). On the gravitational potential of the Earth's
650 lithosphere. *Tectonics*, 13(4), 929–945.

651 Coblenz, D.D. & Sandiford, M. (1994). Tectonic stresses in the African plate: Constraints on the ambi-
652 ent lithospheric stress state. *Geology*, 22(9), 831–834.

653 Debayle, E., Dubuffet, F., & Durand, S. (2016). An automatically updated S-wave model of the upper
654 mantle and the depth extent of azimuthal anisotropy. *Geophysical Research Letters*, 43(2), 674–682.

655 DeMets, C., Gordon, R.G., Argus, D., & Stein, S. (1990). Current plate motions. *Geophysical journal
656 international*, 101(2), 425–478.

657 Dyksterhuis, S. & Müller, R. (2008). Cause and evolution of intraplate orogeny in Australia. *Geology*,
658 36(6), 495–498.

659 Engdahl, E.R., Jackson, J.A., Myers, S.C., Bergman, E.A., & Priestley, K. (2006). Relocation and as-
660 sessment of seismicity in the Iran region. *Geophysical Journal International*, 167(2), 761–778.

661 England, P. & Molnar, P. (1997). Active deformation of Asia: From kinematics to dynamics. *Science*,
662 278(5338), 647–650.

663 Falcon, N.L. (1974). Southern Iran: Zagros Mountains. *Geological Society, London, Special Publica-
664 tions*, 4(1), 199–211.

665 Flesch, L.M., Haines, A.J., & Holt, W.E. (2001). Dynamics of the India-Eurasia collision zone. *Journal
666 of Geophysical Research*, 106(B8), 16435–16460.

667 Flesch, L.M., Holt, W.E., Haines, A.J., Wen, L., & Shen-Tu, B. (2007). The dynamics of western North
668 America: stress magnitudes and the relative role of gravitational potential energy, plate interaction at
669 the boundary and basal tractions. *Geophysical Journal International*, 169(3), 866–896.

670 Franccois, T., Burov, E., Agard, P., & Meyer, B. (2014). Buildup of a dynamically supported oro-
671 genic plateau: Numerical modeling of the Zagros/Central Iran case study. *Geochemistry, Geophysics,
672 Geosystems*, 15(6), 2632–2654.

673 Frohling, E. & Szeliga, W. (2016). GPS constraints on interplate locking within the Makran subduction
674 zone. *Geophysical Supplements to the Monthly Notices of the Royal Astronomical Society*, 205(1),
675 67–76.

676 Gao, Y., Chen, L., Talebian, M., Wu, Z., Wang, X., Lan, H., Ai, Y., Jiang, M., Hou, G., Khatib, M.M.,
677 et al. (2022). Nature and structural heterogeneities of the lithosphere control the continental deforma-
678 tion in the northeastern and eastern Iranian plateau as revealed by shear-wave splitting observations.
679 *Earth and Planetary Science Letters*, 578, 117284.

680 Ghalamghash, J., Bouchez, J., Vosoughi-Abedini, M., & Nédélec, A. (2009). The Urumieh Plutonic
681 Complex (NW Iran): Record of the geodynamic evolution of the Sanandaj–Sirjan zone during Cre-
682 taceous times–Part II: Magnetic fabrics and plate tectonic reconstruction. *Journal of Asian Earth
683 Sciences*, 36(4-5), 303–317.

684 Ghorbani Rostam, G., Pakzad, M., Mirzaei, N., & Sakhaei, S.R. (2018). Analysis of the stress field and
685 strain rate in Zagros-Makran transition zone. *Journal of Seismology*, 22, 287–301.

686 Ghosh, A., Becker, T.W., & Humphreys, E.D. (2013a). Dynamics of the North American continent.
687 *Geophysical Journal International*, 194(2), 651–669.

688 Ghosh, A. & Holt, W.E. (2012). Plate motions and stresses from global dynamic models. *Science*,
689 335(6070), 838–843.

690 Ghosh, A., Holt, W.E., & Flesch, L.M. (2009). Contribution of gravitational potential energy differences
691 to the global stress field. *Geophysical Journal International*, 179(2), 787–812.

692 Ghosh, A., Holt, W.E., & Wen, L. (2013b). Predicting the lithospheric stress field and plate motions by
693 joint modeling of lithosphere and mantle dynamics. *Journal of Geophysical Research: Solid Earth*,
694 118(1), 346–368.

695 Hager, B.H. & O'Connell, R.J. (1981). A simple global model of plate dynamics and mantle convection.
696 *Journal of Geophysical Research*, 86(B6), 4843–4867.

697 Hatzfeld, D., Authemayou, C., van der Beek, P., Bellier, O., Lavé, J., Oveisi, B., Tatar, M., Tavakoli, F.,
698 Walpersdorf, A., & Yamini-Fard, F. (2010). The kinematics of the Zagros mountains (Iran). *Geologi-
699 cal Society, London, Special Publications*, 330(1), 19–42.

700 Hatzfeld, D. & Molnar, P. (2010). Comparisons of the kinematics and deep structures of the Zagros
701 and Himalaya and of the Iranian and Tibetan plateaus and geodynamic implications. *Reviews of Geo-
702 physics*, 48(2).

703 Heidbach, O., Rajabi, M., Reiter, K., & Ziegler, M. (2016). WSM Team (2016): World Stress Map
704 Database Release 2016. *GFZ Data Services*, doi:<http://doi.org/10.5880/WSM.2016.001>.

705 Heidbach, O., Reinecker, J., Tingay, M., Müller, B., Sperner, B., Fuchs, K., & Wenzel, F. (2007). Plate
706 boundary forces are not enough: Second-and third-order stress patterns highlighted in the World Stress
707 Map database. *Tectonics*, 26(6), doi:10.1029/2007TC002133.

708 Hessami, K., Nilforoushan, F., & Talbot, C.J. (2006). Active deformation within the Zagros Mountains
709 deduced from GPS measurements. *Journal of the Geological Society*, 163(1), 143–148.

710 Hirschberg, H.P., Lamb, S., & Savage, M.K. (2018). Strength of an obliquely convergent plate bound-
711 ary: lithospheric stress magnitudes and viscosity in New Zealand. *Geophysical Journal International*,
712 216(2), 1005–1024.

713 Hollingsworth, J., Fattah, M., Walker, R., Talebian, M., Bahroudi, A., Bolourchi, M.J., Jackson, J., &
714 Copley, A. (2010). Oroclinal bending, distributed thrust and strike-slip faulting, and the accommo-
715 dation of Arabia–Eurasia convergence in NE Iran since the Oligocene. *Geophysical Journal Interna-
716 tional*, 181(3), 1214–1246.

717 Irandoust, M.A., Priestley, K., & Sobouti, F. (2022). High-resolution Lithospheric Structure of the Za-
718 gros Collision Zone and Iranian Plateau. *Journal of Geophysical Research: Solid Earth*, 127(11),
719 e2022JB025009, doi:<https://doi.org/10.1029/2022JB025009>.

720 Jackson, J. & McKenzie, D. (1984). Active tectonics of the Alpine—Himalayan Belt between western
721 Turkey and Pakistan. *Geophysical Journal International*, 77(1), 185–264.

722 Jackson, J., Priestley, K., Allen, M., & Berberian, M. (2002). Active tectonics of the south Caspian
723 basin. *Geophysical Journal International*, 148(2), 214–245.

724 Jay, C.N., Flesch, L.M., & Bendick, R.O. (2018). Kinematics and dynamics of the Pamir, Central Asia:
725 Quantifying the roles of continental subduction in force balance. *Journal of Geophysical Research:
726 Solid Earth*, 123(9), 8161–8179.

727 Jolivet, L. & Faccenna, C. (2000). Mediterranean extension and the Africa-Eurasia collision. *Tectonics*,
728 19(6), 1095–1106.

729 Kaviani, A., Hatzfeld, D., Paul, A., Tatar, M., & Priestley, K. (2009). Shear-wave splitting, lithospheric
730 anisotropy, and mantle deformation beneath the Arabia–Eurasia collision zone in Iran. *Earth and
731 Planetary Science Letters*, 286(3-4), 371–378.

732 Kaviani, A., Mahmoodabadi, M., Rümpker, G., Pilia, S., Tatar, M., Nilforoushan, F., Yamini-Fard,
733 F., Moradi, A., & Ali, M.Y. (2021). Mantle-flow diversion beneath the Iranian plateau induced by
734 Zagros’ lithospheric keel. *Scientific reports*, 11(1), 1–12.

735 Khodaverdian, A., Zafarani, H., & Rahimian, M. (2015). Long term fault slip rates, distributed deformation rates and forecast of seismicity in the Iranian Plateau. *Tectonics*, 34(10), 2190–2220.

736

737 Khorrami, F., Vernant, P., Masson, F., Nilfouroushan, F., Mousavi, Z., Nankali, H., Saadat, S.A.,
738 Walpersdorf, A., Hosseini, S., Tavakoli, P., et al. (2019). An up-to-date crustal deformation map
739 of Iran using integrated campaign-mode and permanent GPS velocities. *Geophysical Journal International*,
740 217(2), 832–843.

741 Koptev, A. & Ershov, A. (2010). The role of the gravitational potential of the lithosphere in the formation
742 of a global stress field. *Izvestiya, Physics of the Solid Earth*, 46(12), 1080–1094.

743 Koshnaw, R.I., Stockli, D.F., & Schlunegger, F. (2019). Timing of the Arabia-Eurasia continental colli-
744 sion—Evidence from detrital zircon U-Pb geochronology of the Red Bed Series strata of the northwest
745 Zagros hinterland, Kurdistan region of Iraq. *Geology*, 47(1), 47–50.

746 Kreemer, C., Blewitt, G., & Klein, E.C. (2014). A geodetic plate motion and Global Strain Rate Model.
747 *Geochemistry, Geophysics, Geosystems*, 15(10), 3849–3889.

748 Kustowski, B., Ekström, G., & Dziewoński, A. (2008a). Anisotropic shear-wave velocity structure of
749 the Earth's mantle: A global model. *Journal of Geophysical Research: Solid Earth*, 113(B6).

750 Kustowski, B., Ekström, G., & Dziewoński, A. (2008b). The shear-wave velocity structure in the upper
751 mantle beneath Eurasia. *Geophysical Journal International*, 174(3), 978–992.

752 Laske, G., Masters, G., Ma, Z., & Pasyanos, M. (2013). Update on CRUST1.0 - A 1-degree global
753 model of Earth's crust. *Geophys. Res. Abstr.*, 15, 2658.

754 Le Dertz, K., Meyer, B., Sébrier, M., Nazari, H., Braucher, R., Fattahi, M., Benedetti, L., Foroutan, M.,
755 Siame, L., Bourlès, D., et al. (2009). Holocene right-slip rate determined by cosmogenic and OSL
756 dating on the Anar fault, Central Iran. *Geophysical Journal International*, 179(2), 700–710.

757 Lithgow-Bertelloni, C. & Guynn, J.H. (2004). Origin of the lithospheric stress field. *Journal of Geo-
758 physical Research: Solid Earth*, 109(B1), doi:10.1029/2003JB002467.

759 Masson, F., Anvari, M., Djamour, Y., Walpersdorf, A., Tavakoli, F., Daignieres, M., Nankali, H., &
760 Van Gorp, S. (2007). Large-scale velocity field and strain tensor in Iran inferred from GPS mea-
761 surements: new insight for the present-day deformation pattern within NE Iran. *Geophysical Journal
762 International*, 170(1), 436–440.

763 Masson, F., Djamour, Y., Van Gorp, S., Chèry, J., Tatar, M., Tavakoli, F., Nankali, H., & Vernant, P.
764 (2006). Extension in NW Iran driven by the motion of the South Caspian Basin. *Earth and Planetary*
765 *Science Letters*, 252(1-2), 180–188.

766 Mazhari, S., Bea, F., Amini, S., Ghalamghash, J., Molina, J., Montero, P., Scarrow, J., & Williams, I.
767 (2009). The Eocene bimodal Piranshahr massif of the Sanandaj–Sirjan Zone, NW Iran: a marker of
768 the end of the collision in the Zagros orogen. *Journal of the Geological Society*, 166(1), 53–69.

769 McClusky, S., Balassanian, S., Barka, A., Demir, C., Ergintav, S., Georgiev, I., Gurkan, O., Hamburger,
770 M., Hurst, K., Kahle, H., et al. (2000). Global Positioning System constraints on plate kinematics and
771 dynamics in the eastern Mediterranean and Caucasus. *Journal of Geophysical Research: Solid Earth*,
772 105(B3), 5695–5719.

773 McQuarrie, N., Stock, J., Verdel, C., & Wernicke, B. (2003). Cenozoic evolution of Neotethys and
774 implications for the causes of plate motions. *Geophysical research letters*, 30(20).

775 Md, S.I. & Ryuichi, S. (2010). Neotectonic stress field and deformation pattern within the Zagros and its
776 adjoining area: An approach from finite element modeling. *Journal of Geology and Mining Research*,
777 2(7), 170–182.

778 Mégnin, C. & Romanowicz, B. (2000). The three-dimensional shear velocity structure of the mantle
779 from the inversion of body, surface and higher-mode waveforms. *Geophysical Journal International*,
780 143(3), 709–728.

781 Mohajjal, M. & Fergusson, C.L. (2000). Dextral transpression in Late Cretaceous continental collision,
782 Sanandaj–Sirjan zone, western Iran. *Journal of Structural geology*, 22(8), 1125–1139.

783 Mokhori, A.N., Rahimi, B., & Moayyed, M. (2021). Active tectonic stress field analysis in NW Iran-SE
784 Turkey using earthquake focalmechanism data. *Turkish Journal of Earth Sciences*, 30(2), 235–246.

785 Mouthereau, F., Lacombe, O., & Vergés, J. (2012). Building the Zagros collisional orogen: timing, strain
786 distribution and the dynamics of Arabia/Eurasia plate convergence. *Tectonophysics*, 532, 27–60.

787 Navabpour, P., Angelier, J., & Barrier, E. (2008). Stress state reconstruction of oblique collision and
788 evolution of deformation partitioning in W-Zagros (Iran, Kermanshah). *Geophysical Journal Interna-*
789 *tional*, 175(2), 755–782.

790 Nouri, A., Rahimi, B., Vavryčuk, V., & Ghaemi, F. (2023). Spatially varying crustal stress along the
791 Zagros seismic belt inferred from earthquake focal mechanisms. *Tectonophysics*, 846, 229653.

792 Pasyanos, M.E., Masters, G., Laske, G., & Ma, Z. (2014). LITHO1.0: An updated crust and lithospheric
793 model of the Earth. *Journal of Geophysical Research: Solid Earth*, 119(3), 2153–2173.

794 Raeesi, M., Zarifi, Z., Nilfouroushan, F., Boroujeni, S.A., & Tiampo, K. (2017). Quantitative analysis of
795 seismicity in Iran. *Pure and Applied Geophysics*, 174(3), 793–833.

796 Rashidi, A., Kianimehr, H., Yamini-Fard, F., Tatar, M., & Zafarani, H. (2022). Present Stress Map and
797 Deformation Distribution in the NE Lut Block, Eastern Iran: Insights from Seismic and Geodetic
798 Strain and Moment Rates. *Pure and Applied Geophysics*, 179(5), 1887–1917.

799 Reilinger, R. & McClusky, S. (2011). Nubia–Arabia–Eurasia plate motions and the dynamics of Mediter-
800 ranean and Middle East tectonics. *Geophysical Journal International*, 186(3), 971–979.

801 Reilinger, R., McClusky, S., Paradissis, D., Ergintav, S., & Vernant, P. (2010). Geodetic constraints on
802 the tectonic evolution of the Aegean region and strain accumulation along the Hellenic subduction
803 zone. *Tectonophysics*, 488(1-4), 22–30.

804 Reilinger, R., McClusky, S., Vernant, P., Lawrence, S., Ergintav, S., Cakmak, R., Ozener, H., Kadirov, F.,
805 Guliev, I., Stepanyan, R., Nadariya, M., Hahubia, G., Mahmoud, S., Sakr, K., ArRajehi, A., Paradissis,
806 D., Al-Aydrus, A., Prilepin, M., Guseva, T., Evren, E., Dmitrotsa, A., Filikov, S.V., Gomez, F., Al-
807 Ghazzi, R., & Karamm, G. (2006). GPS constraints on continental deformation in the Africa-Arabia-
808 Eurasia continental collision zone and implications for the dynamics of plate interactions. *Journal of
809 Geophysical Research: Solid Earth*, 111(B5), doi:10.1029/2005JB004051.

810 Richardson, R.M., Solomon, S.C., & Sleep, N.H. (1976). Intraplate stress as an indicator of plate tectonic
811 driving forces. *Journal of geophysical research*, 81(11), 1847–1856.

812 Ritsema, J., Deuss, A.A., Van Heijst, H.J., & Woodhouse, J.H. (2011). S40RTS: a degree-40 shear-
813 velocity model for the mantle from new Rayleigh wave dispersion, teleseismic travelttime and normal-
814 mode splitting function measurements. *Geophysical Journal International*, 184(3), 1223–1236.

815 Robert, A.M., Fernàndez, M., Jiménez-Munt, I., & Vergés, J. (2017). Lithospheric structure in Central
816 Eurasia derived from elevation, geoid anomaly and thermal analysis. *Geological Society, London,
817 Special Publications*, 427(1), 271–293.

818 Sadeghi-Bagherabadi, A., Sobouti, F., Ghods, A., Motaghi, K., Talebian, M., Chen, L., Jiang, M., Ai, Y.,
819 & He, Y. (2018). Upper mantle anisotropy and deformation beneath the major thrust-and-fold belts of
820 Zagros and Alborz and the Iranian Plateau. *Geophysical Journal International*, 214(3), 1913–1918.

821 Sarkarinejad, K., Pash, R.R., Motamedi, H., & Yazdani, M. (2018). Deformation and kinematic evolution
822 of the subsurface structures: Zagros foreland fold-and-thrust belt, northern Dezful Embayment,
823 Iran. *International Journal of Earth Sciences*, 107, 1287–1304.

824 Sattarzadeh, Y., Cosgrove, J.W., & Vita-Finzi, C. (2002). The geometry of structures in the Zagros cover
825 rocks and its neotectonic implications. *Geological Society, London, Special Publications*, 195(1),
826 205–217.

827 Singh, A., Eken, T., Mohanty, D.D., Saikia, D., Singh, C., & Kumar, M.R. (2016). Significant seismic
828 anisotropy beneath southern Tibet inferred from splitting of direct S-waves. *Physics of the Earth and
829 Planetary Interiors*, 250, 1–11.

830 Singh, S. & Ghosh, A. (2019). Surface motions and continental deformation in the Indian plate and
831 the India-Eurasia collision zone. *Journal of Geophysical Research: Solid Earth*, 124, doi:10.1029/
832 2018JB017289.

833 Singh, S. & Ghosh, A. (2020). The role of crustal models in the dynamics of the India–Eurasia collision
834 zone. *Geophysical Journal International*, 223(1), 111–131.

835 Sobouti, F. & Arkani-Hamed, J. (1996). Numerical modelling of the deformation of the Iranian plateau.
836 *Geophysical Journal International*, 126(3), 805–818.

837 Sol, S., Meltzer, A., Burgmann, R., Van der Hilst, R., King, R., Chen, Z., Koons, P., Lev, E., Liu, Y.,
838 Zeitler, P., et al. (2007). Geodynamics of the southeastern Tibetan Plateau from seismic anisotropy
839 and geodesy. *Geology*, 35(6), 563–566.

840 Steinberger, B. & Holme, R. (2008). Mantle flow models with core-mantle boundary constraints and
841 chemical heterogeneities in the lowermost mantle. *Journal of Geophysical Research: Solid Earth*,
842 113(B5), doi:10.1029/2007JB005080.

843 Talebian, M. & Jackson, J. (2002). Offset on the Main Recent Fault of NW Iran and implications for
844 the late Cenozoic tectonics of the Arabia–Eurasia collision zone. *Geophysical Journal International*,
845 150(2), 422–439.

846 Tatar, M. & Hatzfeld, D. (2009). Microseismic evidence of slip partitioning for the Rudbar-Tarom earth-
847 quake (Ms 7.7) of 1990 June 20 in NW Iran. *Geophysical Journal International*, 176(2), 529–541.

848 Tunini, L., Jiménez-Munt, I., Fernandez, M., Vergés, J., & Bird, P. (2017). Neotectonic deformation
849 in central Eurasia: A geodynamic model approach. *Journal of Geophysical Research: Solid Earth*,
850 122(11), 9461–9484.

851 Tunini, L., Jiménez-Munt, I., Fernandez, M., Vergés, J., Villaseñor, A., Melchiorre, M., & Afonso, J.C.
852 (2016). Geophysical-petrological model of the crust and upper mantle in the India-Eurasia collision
853 zone. *Tectonics*, 35(7), 1642–1669.

854 Vernant, P. & Chéry, J. (2006). Mechanical modelling of oblique convergence in the Zagros, Iran. *Geo-*
855 *physical Journal International*, 165(3), 991–1002.

856 Vernant, P., Nilforoushan, F., Hatzfeld, D., Abbassi, M., Vigny, C., Masson, F., Nankali, H., Martinod,
857 J., Ashtiani, A., Bayer, R., et al. (2004). Present-day crustal deformation and plate kinematics in
858 the Middle East constrained by GPS measurements in Iran and northern Oman. *Geophysical Journal*
859 *International*, 157(1), 381–398.

860 Vincent, S.J., Allen, M.B., Ismail-Zadeh, A.D., Flecker, R., Foland, K.A., & Simmons, M.D. (2005).
861 Insights from the Talysh of Azerbaijan into the Paleogene evolution of the South Caspian region.
862 *Geological Society of America Bulletin*, 117(11-12), 1513–1533.

863 Walker, R.T. (2006). A remote sensing study of active folding and faulting in southern Kerman province,
864 SE Iran. *Journal of Structural Geology*, 28(4), 654–668.

865 Walpersdorf, A., Hatzfeld, D., Nankali, H., Tavakoli, F., Nilforoushan, F., Tatar, M., Vernant, P., Chéry,
866 J., & Masson, F. (2006). Difference in the GPS deformation pattern of North and Central Zagros
867 (Iran). *Geophysical Journal International*, 167(3), 1077–1088.

868 Walpersdorf, A., Manighetti, I., Mousavi, Z., Tavakoli, F., Vergnolle, M., Jadidi, A., Hatzfeld, D.,
869 Aghamohammadi, A., Bigot, A., Djamour, Y., et al. (2014). Present-day kinematics and fault slip
870 rates in eastern Iran, derived from 11 years of GPS data. *Journal of Geophysical Research: Solid*
871 *Earth*, 119(2), 1359–1383.

872 Yadav, R. & Tiwari, V. (2018). Numerical simulation of present day tectonic stress across the Indian
873 subcontinent. *International Journal of Earth Sciences*, 107(7), 2449–2462.

874 Yaghoubi, A., Mahbaz, S., Dusseault, M.B., & Leonenko, Y. (2021). Seismicity and the state of stress
875 in the Dezful embayment, Zagros fold and thrust belt. *Geosciences*, 11(6), 254.

876 Yamato, P., Kaus, B.J., Mouthereau, F., & Castelltort, S. (2011). Dynamic constraints on the crustal-scale
877 rheology of the Zagros fold belt, Iran. *Geology*, 39(9), 815–818.

878 Yang, Y., Liang, C., Fang, L., Su, J., & Hua, Q. (2018). A comprehensive analysis on the stress field and
879 seismic anisotropy in eastern Tibet. *Tectonics*, 37(6), 1648–1657.

880 Zoback, M.L. (1992). First-and second-order patterns of stress in the lithosphere: The World Stress Map
881 Project. *Journal of Geophysical Research: Solid Earth*, 97(B8), 11703–11728.

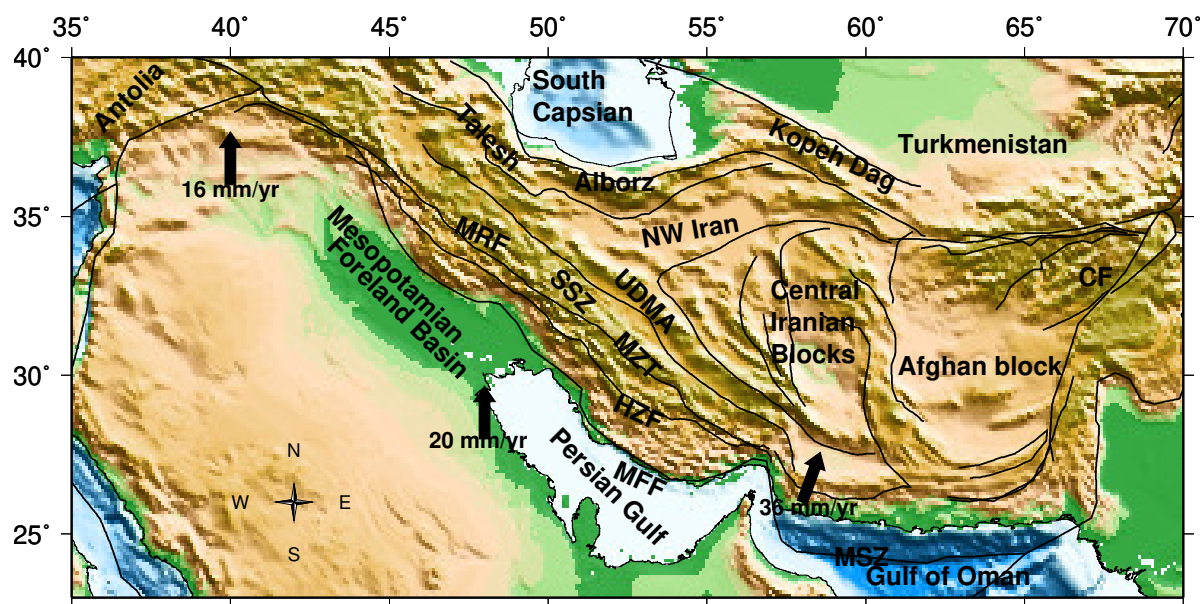


Figure 1: Tectonic overview of Central Eurasia. Abbreviations: CF: Chaman Fault; MSZ: Makran Subduction Zone; MZT: Main Zagros Thrust; HZF: High Zagros Fault; MFF: Mountain Front Fault; SSZ: Sanandaj Sirjan Zone; UDMA: Urumieh-Dokhtar Arc; MRF: Main Recent Fault.

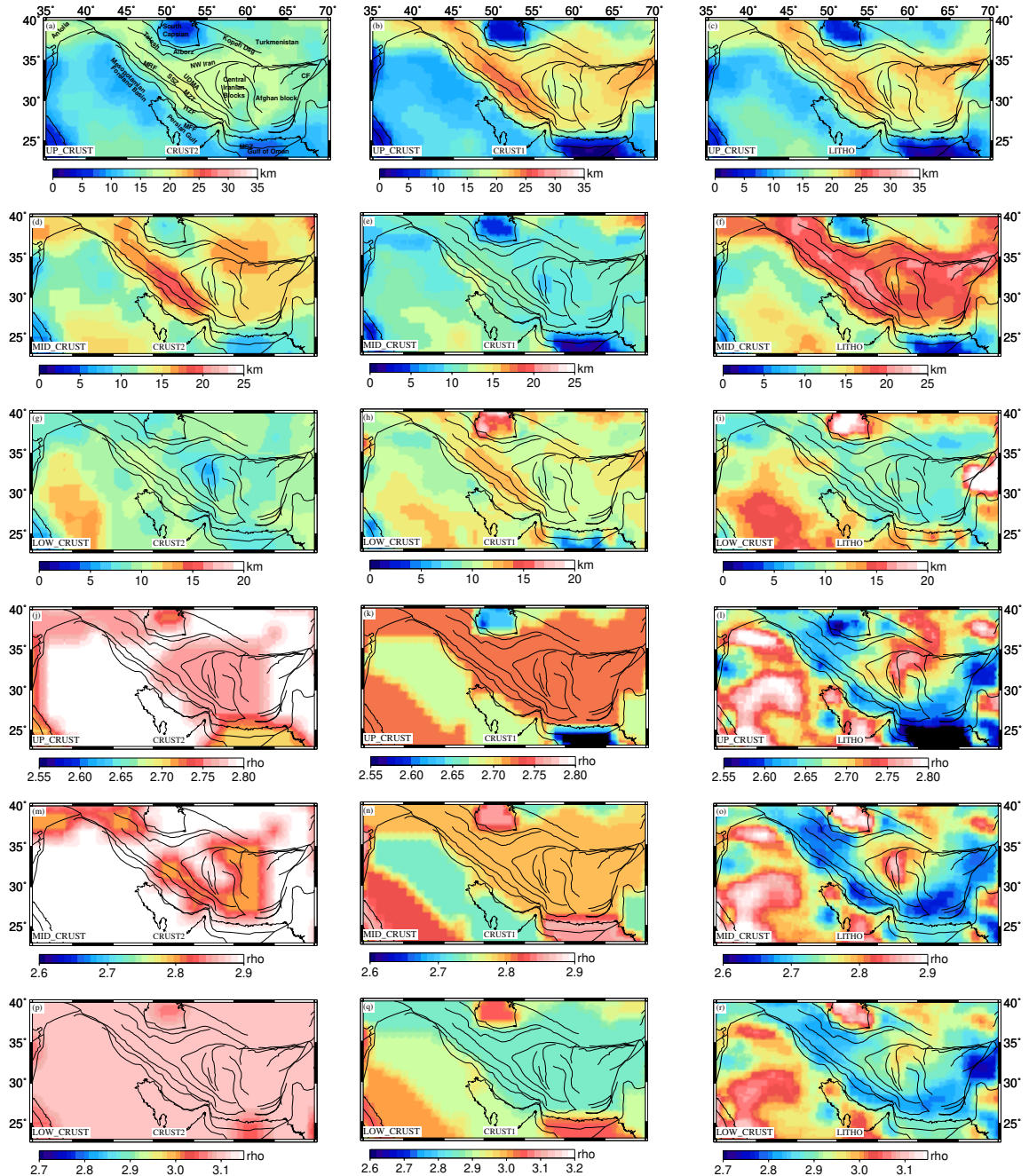


Figure 2: Thickness and density variations of different layers in all three crustal and lithospheric models: CRUST2(Left panel), CRUST1(Middle Panel) and LITHO1(Right panel)

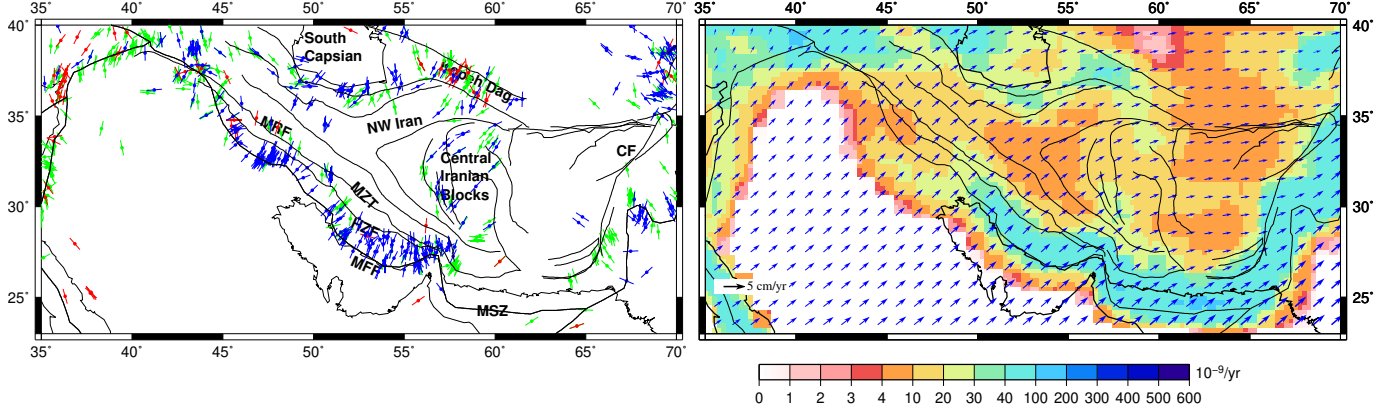


Figure 3: (a) Most compressive horizontal principal axes (S_{Hmax}) from WSM (Heidbach et al., 2016). Red indicates normal fault regime, blue indicates thrust regime, whereas green denotes strike-slip regime, (b) Observed plate velocities in a no-net-rotation frame of reference from Kreemer et al. (2014) plotted on top of second invariant of strain rate tensors obtained from Kreemer et al. (2014) plotted on $1^\circ \times 1^\circ$ grid.

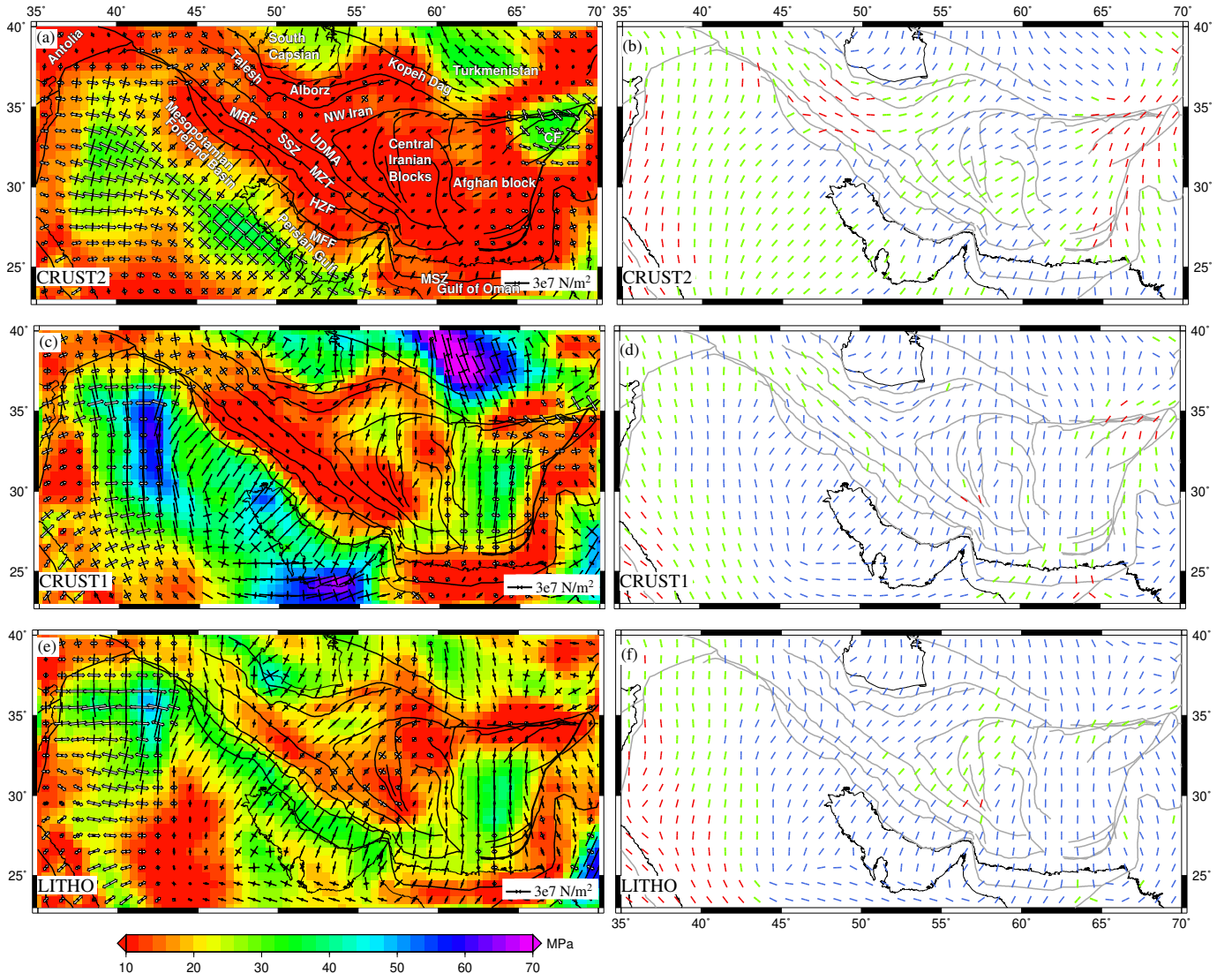


Figure 4: (Left Panel) Deviatoric stresses predicted from GPE variations, plotted on top of their second invariants. The compressional stresses are denoted by solid black arrows, while white arrows show tensional stresses. S_{Hmax} axes predicted from GPE variations are plotted in right panel. Red denotes tensional regime, blue is for thrust and green for strike-slip regime.

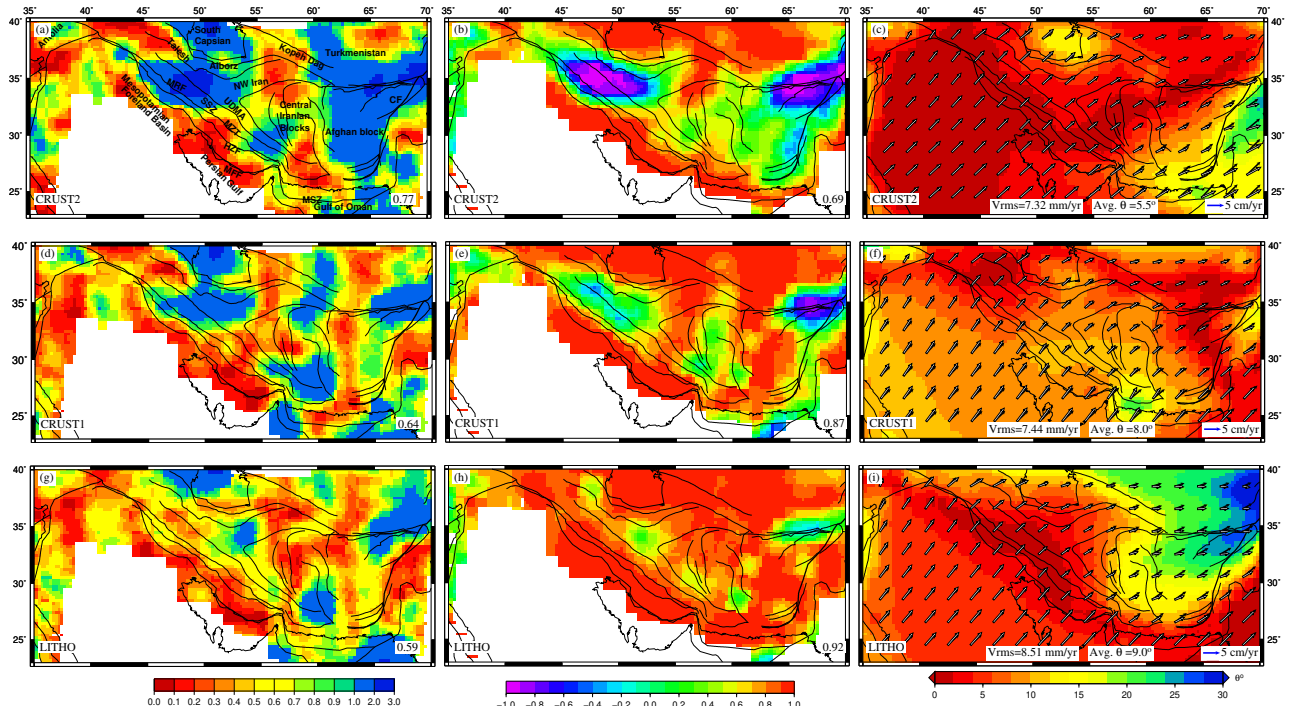


Figure 5: (Left Panel) Total misfit between observed and predicted $S_{H\max}$ from GPE variations. Correlation coefficients between strain rate tensors obtained from Kreemer et al. (2014) and deviatoric stresses predicted using GPE variations are shown in middle panel, with average regional correlation coefficients given on bottom right of each figure. (Right panel) Observed velocities (black) and predicted plate velocities(white) from GPE variations in NNR frame, plotted on the top of angular misfit between both.

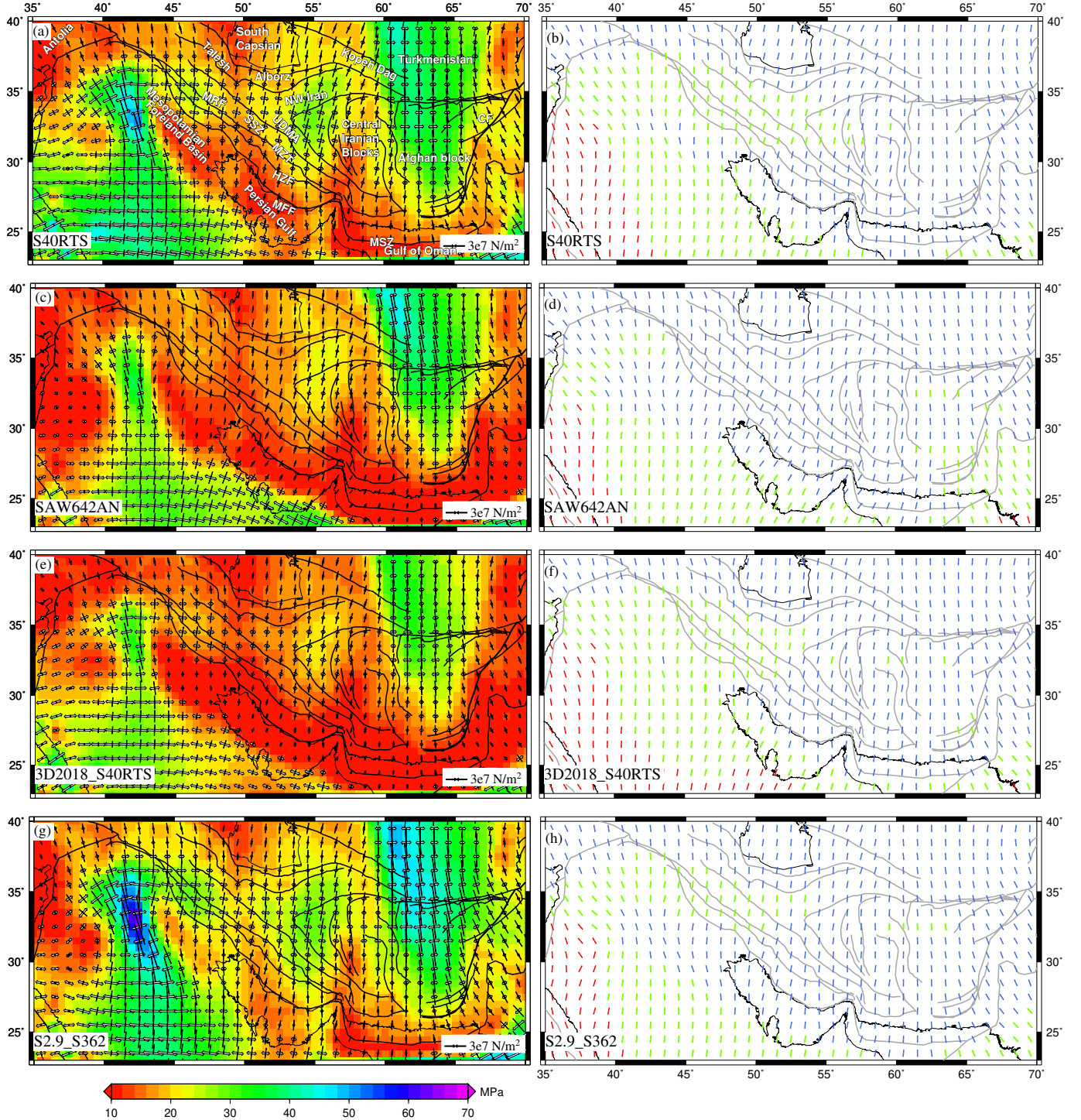


Figure 6: (Left Panel) Deviatoric stresses predicted using mantle tractions derived from various tomography models for GHW13 viscosity structure, plotted on second invariant of deviatoric stresses. The white arrows denote tensional stresses, and black arrows indicate compressional stresses. S_{Hmax} predicted from mantle tractions are shown in right panel. Red denotes tensional regime, blue is for thrust and green is for strike-slip regime.

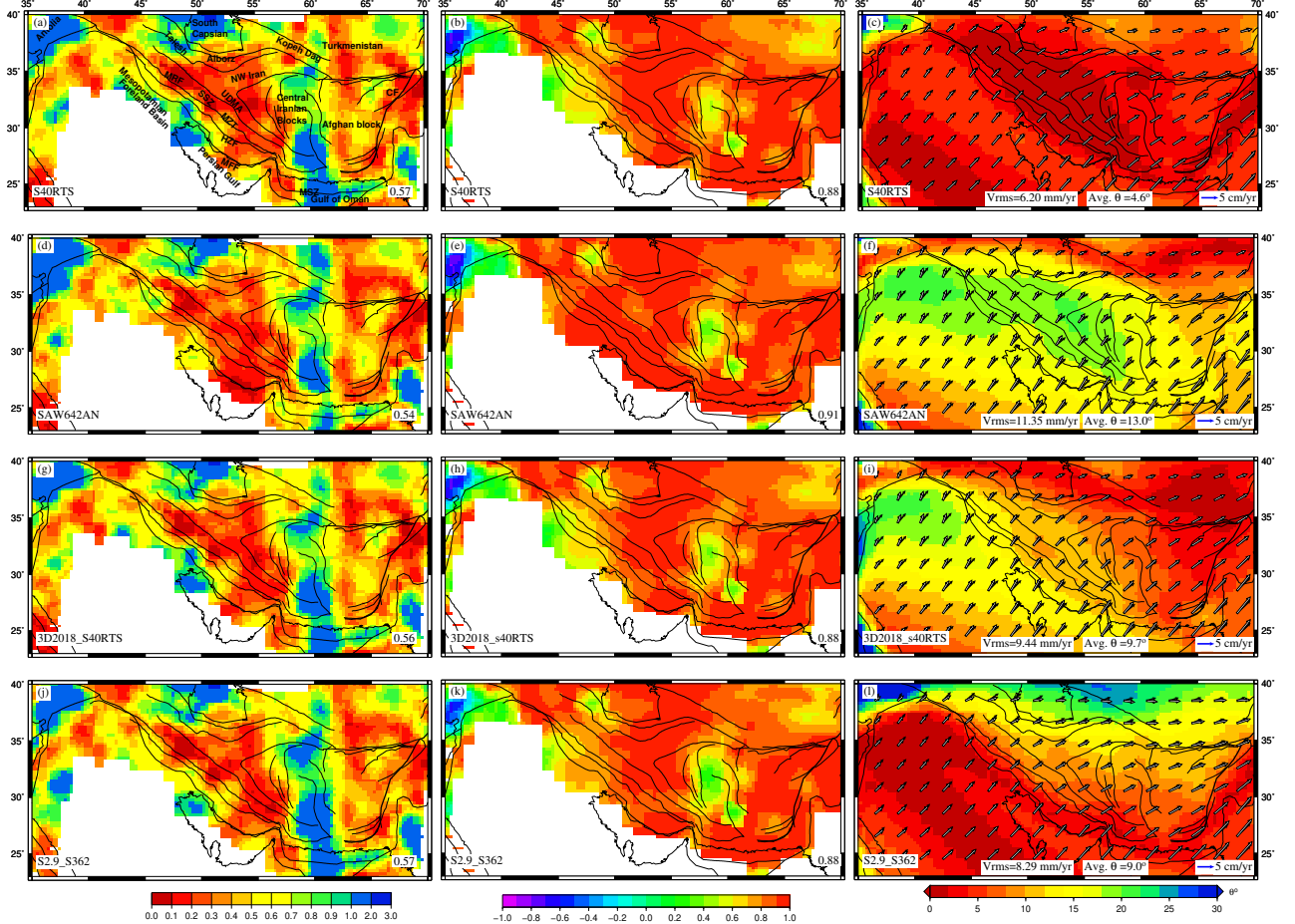


Figure 7: Parameters predicted from mantle tractions and their comparisons with observables. (Left panel) Total misfit between $S_{H\max}$ obtained from WSM (Heidbach et al., 2016) and those predicted using mantle tractions derived from various tomography models using GHW13 viscosity structure. Correlation coefficients between strain rate tensors obtained from Kreemer et al. (2014) and deviatoric stresses predicted using basal tractions are shown in middle panel, with average regional correlation coefficients given on bottom right of each figure. (Right pannel) Observed velocities (black) and plate velocities predicted using mantle tractions (white) in NNR frame plotted on the top of angular deviation between both.

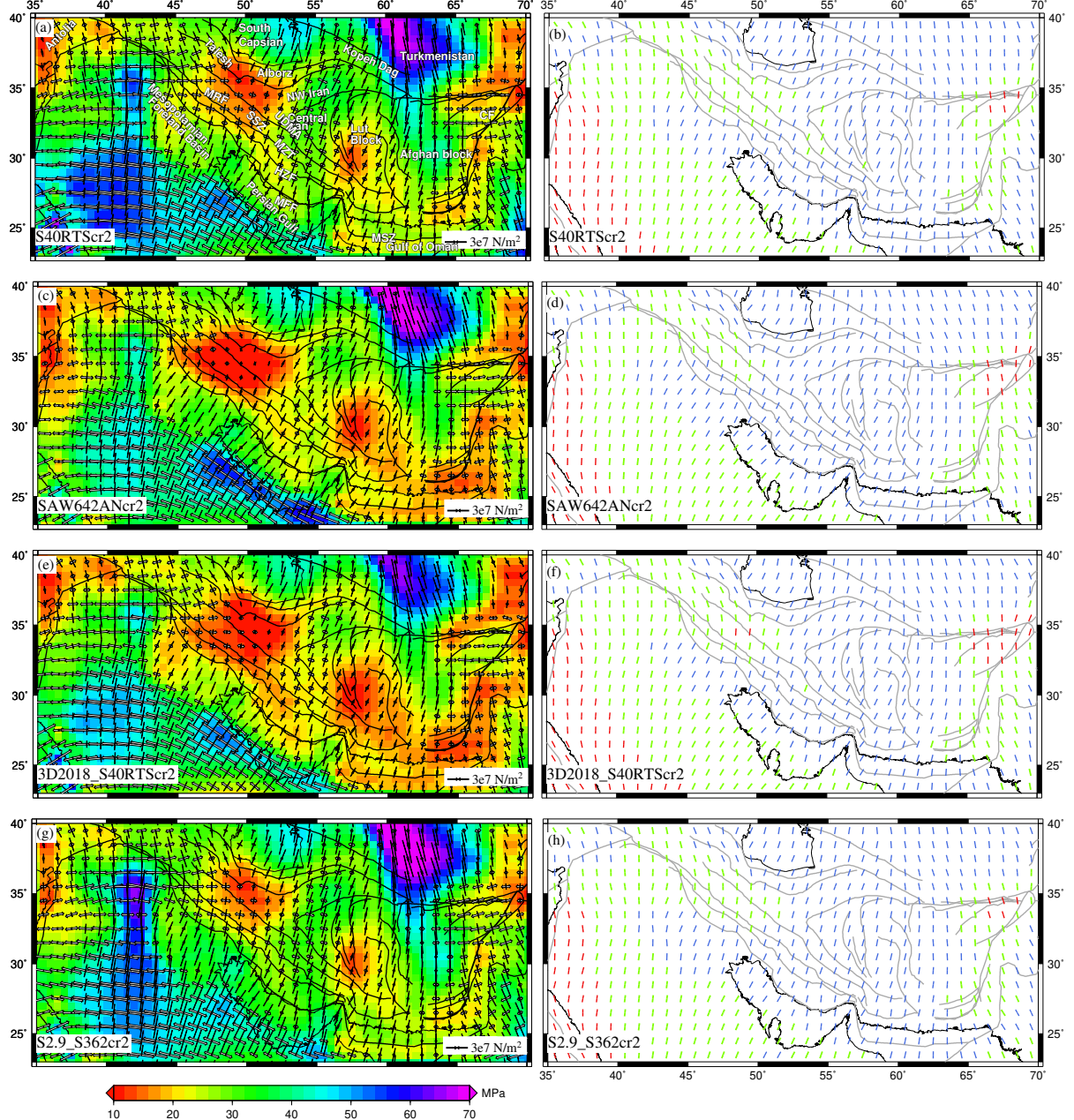


Figure 8: (Left panel) Deviatoric stresses predicted using combined effects of GPE computed from CRUST2 and mantle tractions derived from various tomography models plotted on top of their second invariants. The white arrows denote tensional stresses, and black arrows indicate compressional stresses. The right panel shows S_{Hmax} predicted from these models. The red lines denote tensional regime, blue is for thrust and green is for strike-slip regime.

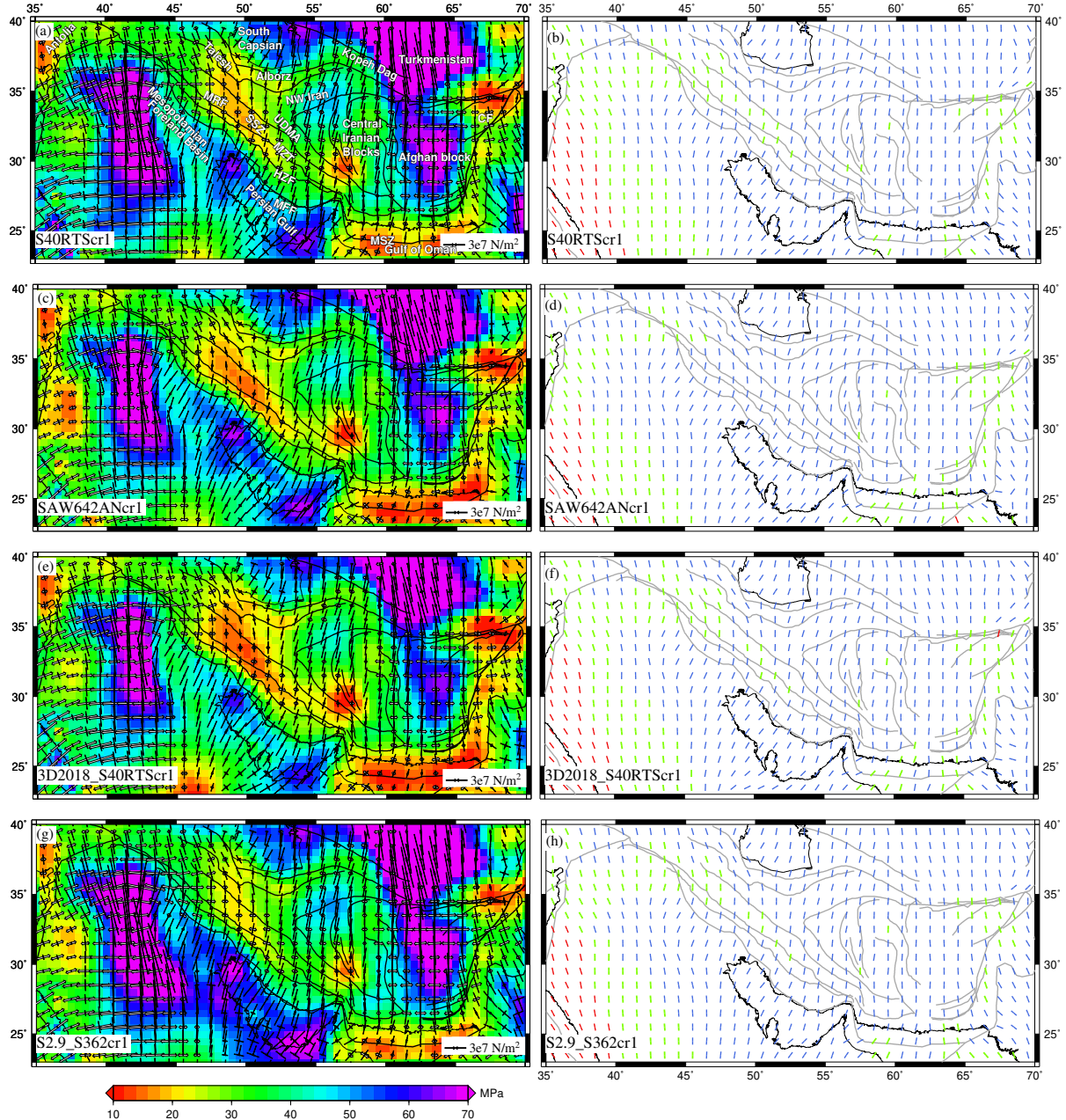


Figure 9: (Left panel) Deviatoric stresses (a-d) predicted using combined effects of GPE computed from CRUST1 and mantle tractions derived from various tomography models plotted on top of their second invariants. The white arrows denote tensional stresses, and black arrows indicate compressional stresses. The right panel shows $S_{H\max}$ predicted from these models. The red lines denote tensional regime, blue is for thrust and green is for strike-slip regime.

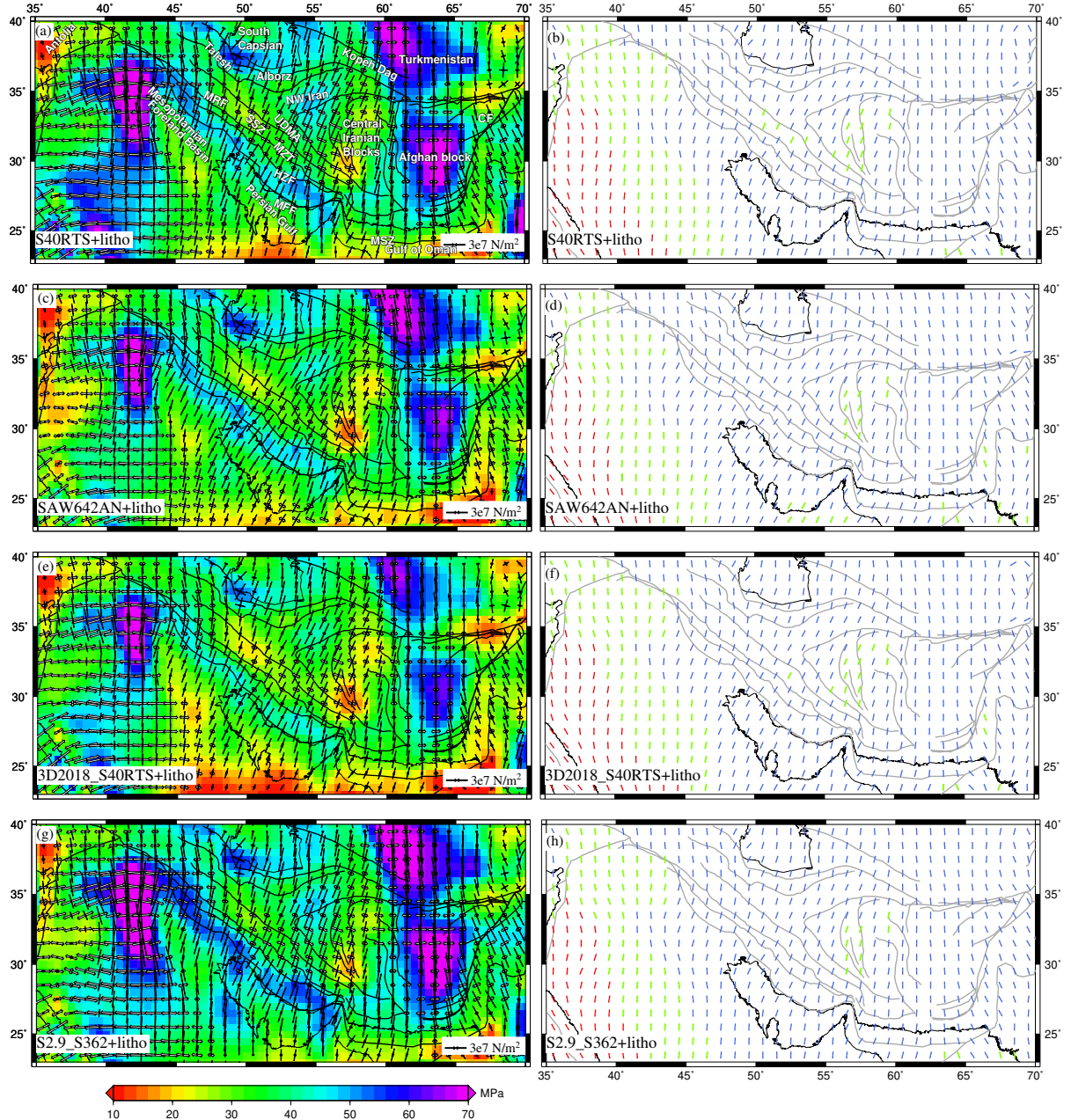


Figure 10: (Left panel) Deviatoric stresses (a-d) predicted using combined effects of GPE computed from LITHO and mantle tractions derived from various tomography models plotted on top of their second invariants. The white arrows denote tensional stresses, and black arrows indicate compressional stresses. The right panel shows S_{Hmax} predicted from these models. The red lines denote tensional regime, blue is for thrust and green is for strike-slip regime.

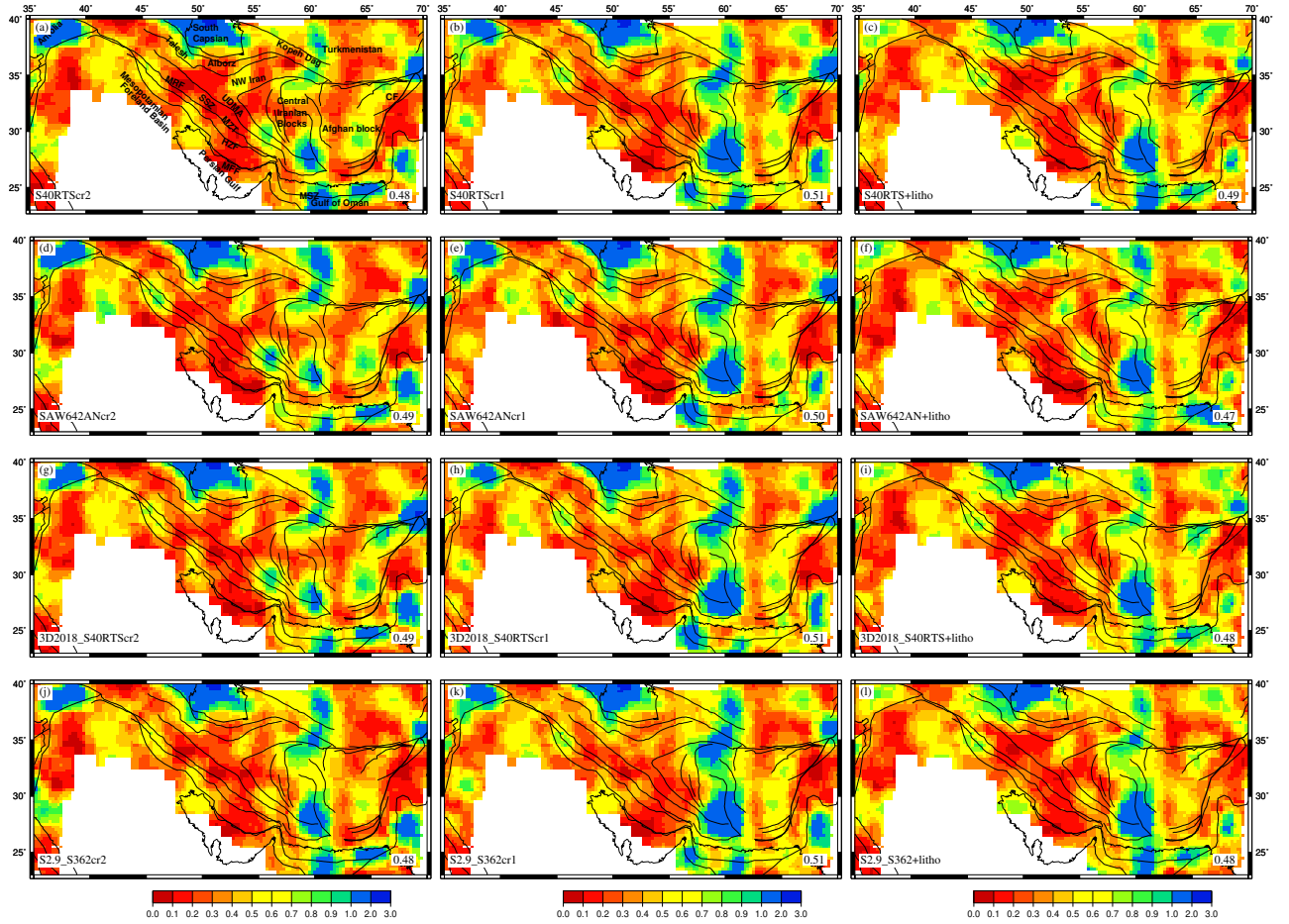


Figure 11: Total misfit between observed $S_{H\max}$ from WSM (Heidbach et al., 2016) and $S_{H\max}$ predicted using combined effects of GPE computed from different crustal models and mantle tractions derived from various tomography models.

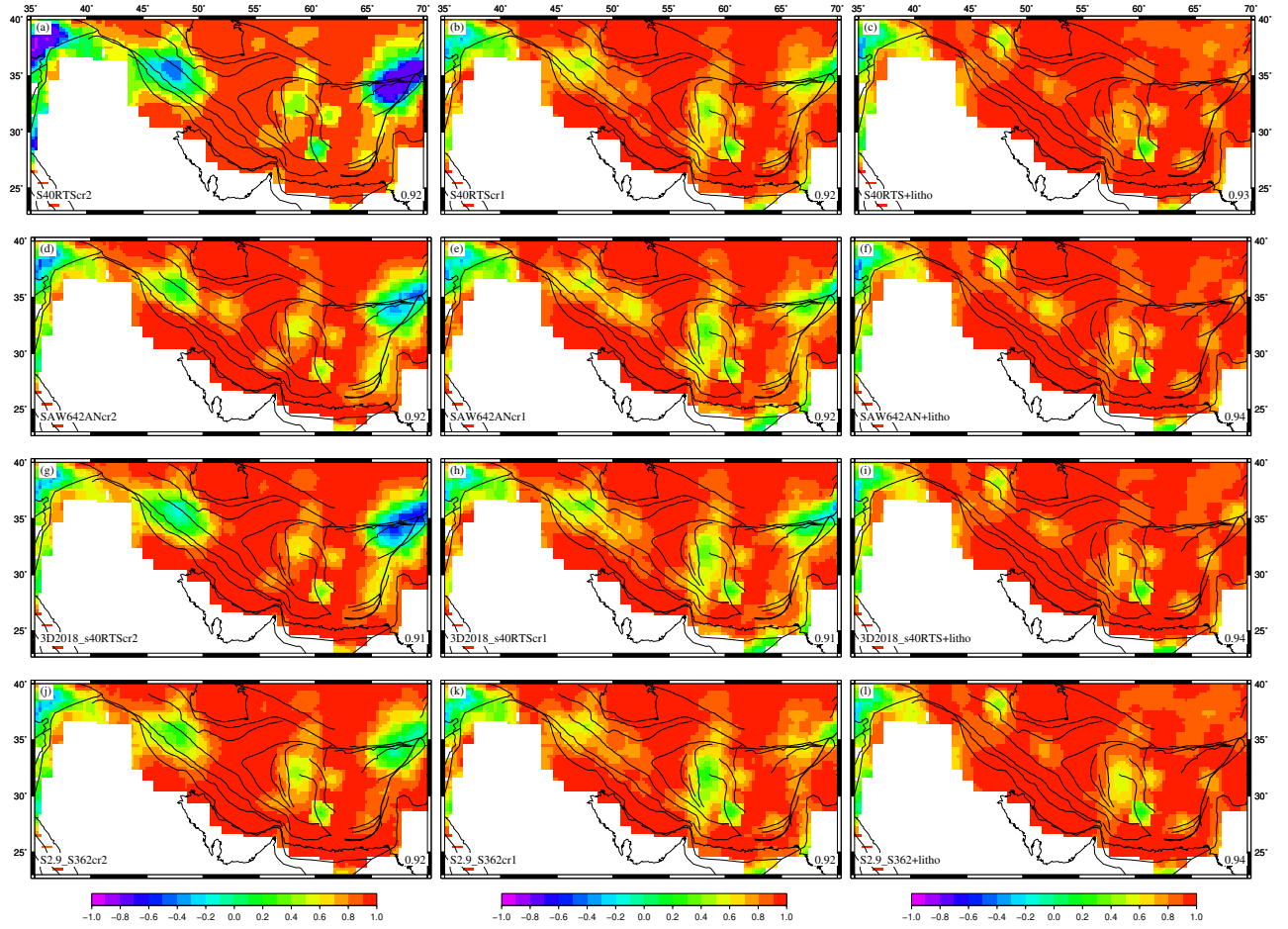


Figure 12: Correlation coefficients between strain rate tensors from Kreemer et al. (2014) and deviatoric stress tensors predicted using combined effects of GPE computed from different crustal models and mantle tractions derived from various tomography models. Average correlation coefficient is given in right lower corner of the figure.

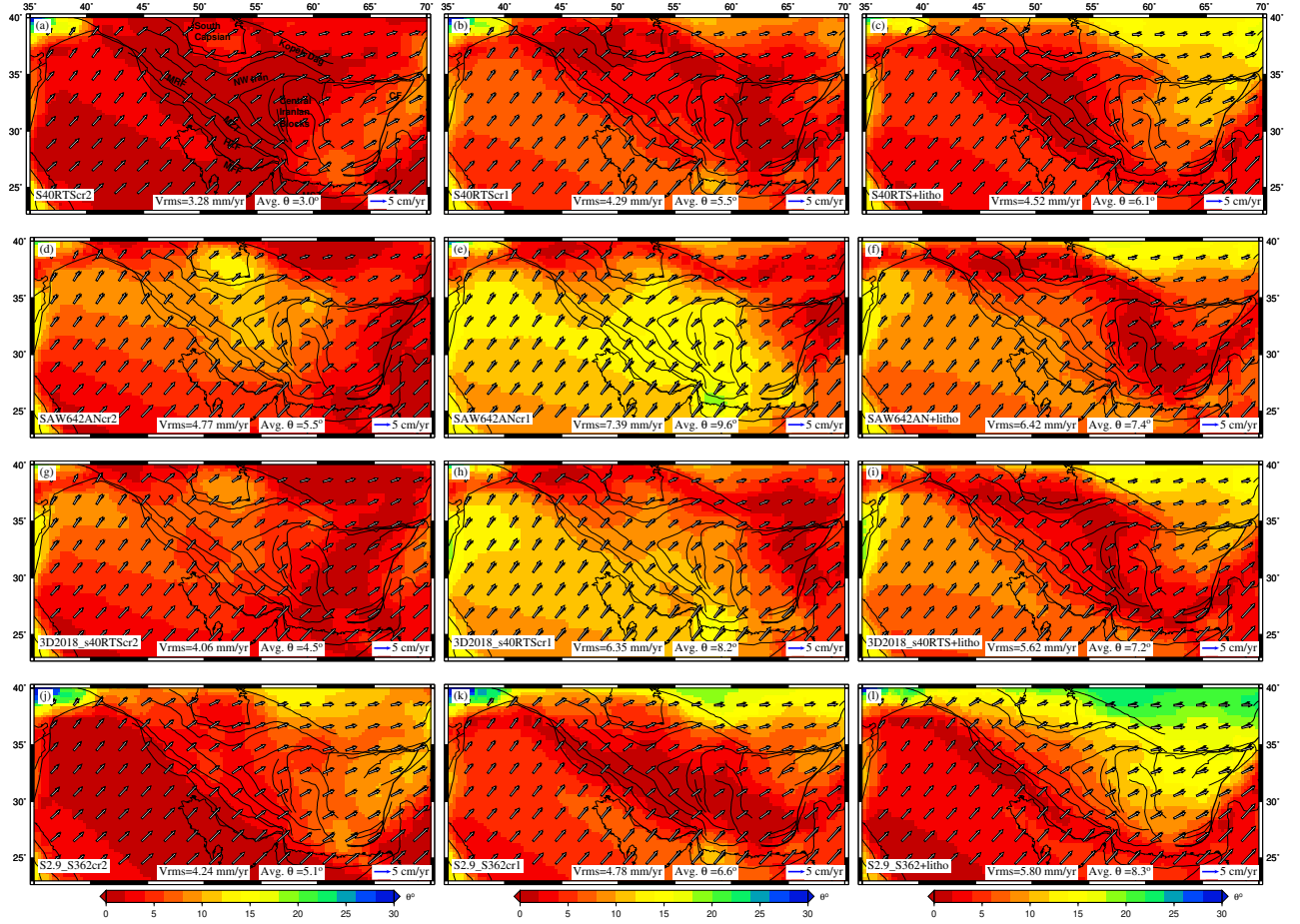


Figure 13: Plate velocities predicted using combined effects of GPE computed from different crustal models and mantle tractions derived from various tomography models plotted on top of angular misfit (θ). Black arrows represent observed NNR velocities (Kreemer et al., 2014) and white ones denote predicted velocities.

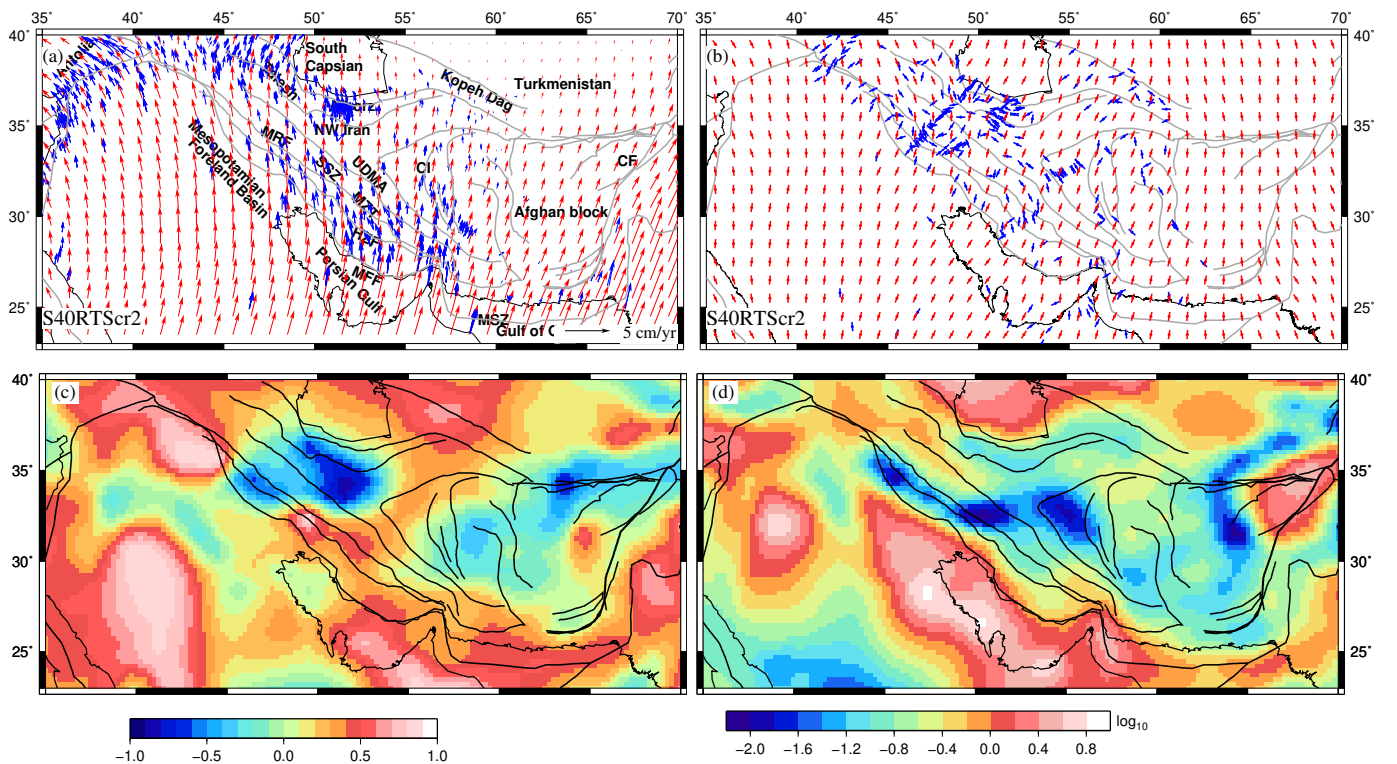


Figure 14: Predicted parameters of best fit model, S40RTScr2. (a) GPS (blue) and predicted (red) plate velocities with respect to a fixed Eurasian plate, (b) FPDs (blue) and S_{Hmax} (red) are plotted for the best fit model, (c) Correlation between deviatoric stresses predicted from GPE and mantle convection models, and (d) ratio (T_1/T_2) of second invariant of deviatoric stresses from GPE (T_1) to those from mantle tractions (T_2).

Supplementary Materials

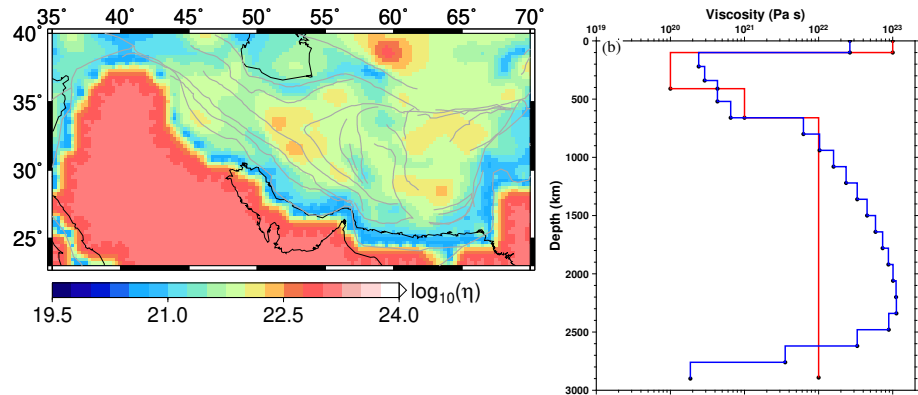


Figure S1: (Left) Plot of lithospheric viscosity in the study region that is used in finite element models. Right panel shows GHW13(red) and SH08 (blue) viscosity structures used in mantle convection models.

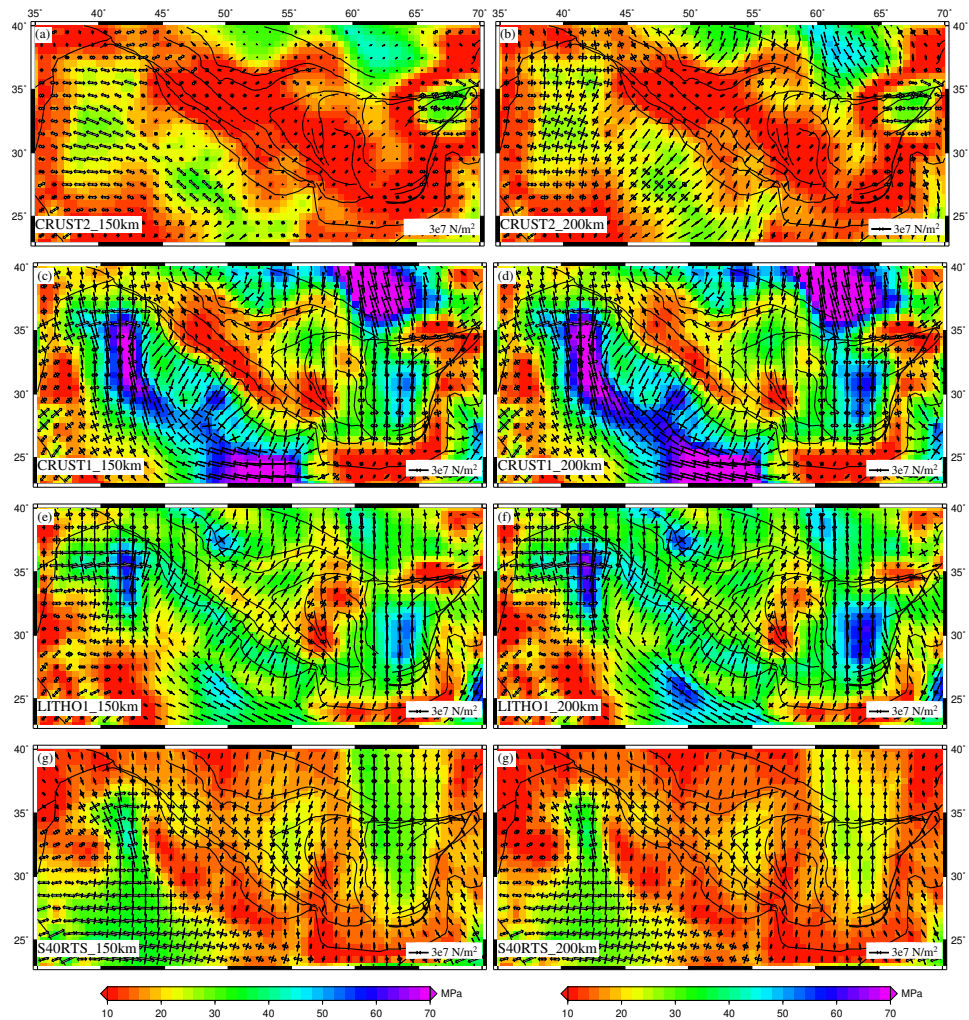


Figure S2: (a-f) Deviatoric stresses predicted using GPE models for lithosphere base at 150 km (left) and 200 km (right). (g-h) Mantle derived stresses from S40RTS tomography model for GHW13 viscosity structures, when LAB is at 150 km (left) and 200 km (right). The background plot shows the second invariant of deviatoric stresses. The white arrows denote tensional stresses, and black arrows indicate compressional stresses.

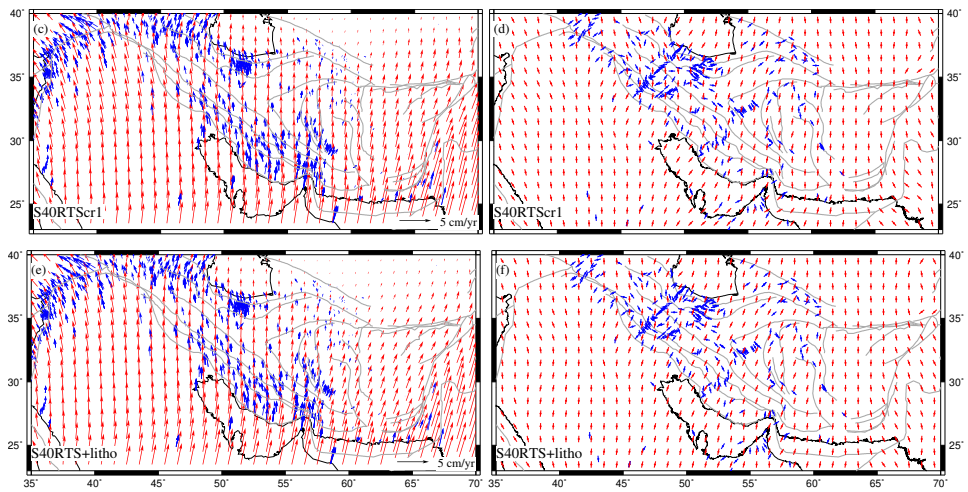


Figure S3: (Left Panel) GPS (blue) and predicted (red) plate velocities with respect to a fixed Eurasian plate. Right Panel shows plot of FPDs in blue and $S_{H\max}$ in red.

Table S1: Summary of quantitative comparison of predicted results of various models with observed data for SH08 viscosity model (Steinberger & Holme, 2008).

Model	SHmax misfit	Strain rate correlation	RMS error (mm/yr)	Angular misfit	Total error
S40RTS+SH08	0.58	0.9	5.68	6	2.42
SAW642AN+SH08	0.58	0.88	17.41	22	3.56
3D2018_S40RTS+SH08	0.58	0.88	8.68	9.2	2.86
S2.9_S363+SH08	0.54	0.89	10.38	14	2.99
S40RTS+SH08cr2	0.52	0.91	3.81	3.3	1.95
SAW642AN+SH08cr2	0.56	0.89	5.38	5.1	2.35
3D2018_S40RTS+SH08cr2	0.54	0.89	4.15	3.3	2.07
S2.9_S362+SH08cr2	0.52	0.92	5.14	5.8	2.24
S40RTS+SH08cr1	0.54	0.92	4.8	6.1	2.19
SAW642AN+SH08cr1	0.54	0.91	8.61	10.7	2.78
3D2018_S40RTS+SH08cr1	0.56	0.91	6.3	7.9	2.49
S2.9_S362+SH08cr1	0.55	0.91	5.82	7.6	2.40
S40RTS+SH08+litho	0.52	0.94	5.79	7.4	2.34
SAW642AN+SH08+litho	0.51	0.94	8.05	8.7	2.66
3D2018_S40RTS+SH08+litho	0.53	0.94	6.61	8.2	2.48
S2.9_S362+SH08+litho	0.53	0.94	7.61	10.1	2.62

Table S2: Quantitative comparison of fit to the observed data for varying LAB depths.

Model/LAB Depth	S _{Hmax} error			Strain Rates Correlation			Velocity rms error		
	100 km	150 km	200 km	100 km	150 km	200 km	100 km	150 km	200 km
CRUST2	0.77	0.64	0.6	0.69	0.83	0.87	7.32	5.85	5.69
CRUST1	0.64	0.61	0.6	0.87	0.9	0.9	7.44	8.59	9.28
LITHO1	0.59	0.56	0.56	0.92	0.93	0.93	8.51	9.03	9.45
S40RTS	0.57	0.56	0.54	0.88	0.89	0.9	6.2	5.9	6.06
S40RTScr2	0.48	0.48	0.49	0.92	0.92	0.93	3.28	5.24	3.82
S40RTScr1	0.51	0.52	0.53	0.92	0.92	0.92	4.29	9.6	9.28
S40RTS+litho1	0.49	0.5	0.51	0.93	0.93	0.94	4.52	9.03	9.45